

AFRL-AFOSR-UK-TR-2014-0001



**Theoretical-Numerical Analysis of Boundary-Layer Stability
with Combined Injection and Acoustic Absorptive Coating**

Alexander V. Fedorov and Vitaly G. Soudakov

**Moscow Institute of Physics and Technology
9, Institutskii per.
Dolgoprudny, Moscow Region, 141700
Russia**

EOARD FA9550-12-D-0003 0002/CRDF 12-2044

Report Date: January 2014

Final Report from 01 November 2012 to 30 January 2014

Distribution Statement A: Approved for public release distribution is unlimited.

**Air Force Research Laboratory
Air Force Office of Scientific Research
European Office of Aerospace Research and Development
Unit 4515, APO AE 09421-4515**

REPORT DOCUMENTATION PAGE

Form Approved OMB No. 0704-0188

Public reporting burden for this collection of information is estimated to average 1 hour per response, including the time for reviewing instructions, searching existing data sources, gathering and maintaining the data needed, and completing and reviewing the collection of information. Send comments regarding this burden estimate or any other aspect of this collection of information, including suggestions for reducing the burden, to Department of Defense, Washington Headquarters Services, Directorate for Information Operations and Reports (0704-0188), 1215 Jefferson Davis Highway, Suite 1204, Arlington, VA 22202-4302. Respondents should be aware that notwithstanding any other provision of law, no person shall be subject to any penalty for failing to comply with a collection of information if it does not display a currently valid OMB control number.
PLEASE DO NOT RETURN YOUR FORM TO THE ABOVE ADDRESS.

1. REPORT DATE (DD-MM-YYYY) 24 January 2014	2. REPORT TYPE Final Report	3. DATES COVERED (From – To) 1 November 2012 – 30 January 2014
---	---------------------------------------	--

4. TITLE AND SUBTITLE Theoretical-Numerical Analysis of Boundary-Layer Stability with Combined Injection and Acoustic Absorptive Coating	<table border="1" style="width:100%; border-collapse: collapse;"> <tr> <td>5a. CONTRACT NUMBER FA9550-12-D-0003 0002</td> </tr> <tr> <td>5b. GRANT NUMBER CRDF 12-2044</td> </tr> <tr> <td>5c. PROGRAM ELEMENT NUMBER 61102F</td> </tr> </table>	5a. CONTRACT NUMBER FA9550-12-D-0003 0002	5b. GRANT NUMBER CRDF 12-2044	5c. PROGRAM ELEMENT NUMBER 61102F
5a. CONTRACT NUMBER FA9550-12-D-0003 0002				
5b. GRANT NUMBER CRDF 12-2044				
5c. PROGRAM ELEMENT NUMBER 61102F				

6. AUTHOR(S) Alexander V. Fedorov and Vitaly G. Soudakov	<table border="1" style="width:100%; border-collapse: collapse;"> <tr> <td>5d. PROJECT NUMBER</td> </tr> <tr> <td>5d. TASK NUMBER</td> </tr> <tr> <td>5e. WORK UNIT NUMBER</td> </tr> </table>	5d. PROJECT NUMBER	5d. TASK NUMBER	5e. WORK UNIT NUMBER
5d. PROJECT NUMBER				
5d. TASK NUMBER				
5e. WORK UNIT NUMBER				

7. PERFORMING ORGANIZATION NAME(S) AND ADDRESS(ES) Moscow Institute of Physics and Technology 9, Institutskii per. Dolgoprudny, Moscow Region, 141700 Russia	8. PERFORMING ORGANIZATION REPORT NUMBER N/A
---	--

9. SPONSORING/MONITORING AGENCY NAME(S) AND ADDRESS(ES) Oleksiy Fomin, U.S. CRDF, Representative Office in Ukraine, 4 Bogomoltsa Str., 134, Kyiv 01024 Ukraine EOARD, Unit 4515 APO AE 09421-4515	<table border="1" style="width:100%; border-collapse: collapse;"> <tr> <td>10. SPONSOR/MONITOR'S ACRONYM(S) AFRL/AFOSR/IOE (EOARD)</td> </tr> <tr> <td>11. SPONSOR/MONITOR'S REPORT NUMBER(S) AFRL-AFOSR-UK-TR-2014-0001</td> </tr> </table>	10. SPONSOR/MONITOR'S ACRONYM(S) AFRL/AFOSR/IOE (EOARD)	11. SPONSOR/MONITOR'S REPORT NUMBER(S) AFRL-AFOSR-UK-TR-2014-0001
10. SPONSOR/MONITOR'S ACRONYM(S) AFRL/AFOSR/IOE (EOARD)			
11. SPONSOR/MONITOR'S REPORT NUMBER(S) AFRL-AFOSR-UK-TR-2014-0001			

12. DISTRIBUTION/AVAILABILITY STATEMENT

Distribution A: Approved for public release; distribution is unlimited.

13. SUPPLEMENTARY NOTES

14. ABSTRACT

This report summarizes results of stability analyses performed for a slender sharp cone with and without injection of air through a porous strip. The free-stream parameters are related to the experiments in the Caltech's T5 shock tunnel. The analysis is focused on pure aerodynamic effects in the framework of perfect gas model. It was shown that the injection leads to destabilization of acoustic modes in the near-field relaxation region. To reduce this detrimental effect it was suggested to alter the injector surface shape or use suction-blowing of zero net injection. However, stability computations showed that these modifications did not improve the injector performance. The porous wall effect on the acoustic instability was also examined. It was found that porosity stabilizes the boundary layer flow with and without injection. This indicates that the injector performance can be improved, if the porous layer, which is used for the injection, is protruded downstream to cover the near-filed relaxation region.

15. SUBJECT TERMS

EOARD, Boundary Layer, BL absorption, BL stability, BL injeuction, hyperconic BL

16. SECURITY CLASSIFICATION OF:			17. LIMITATION OF ABSTRACT SAR	18. NUMBER OF PAGES 44	19a. NAME OF RESPONSIBLE PERSON Gregg Abate
a. REPORT UNCLAS	b. ABSTRACT UNCLAS	c. THIS PAGE UNCLAS			19b. TELEPHONE NUMBER (Include area code) +44 (0)1895 616021

Theoretical-Numerical Analysis of Boundary-Layer Stability with Combined Injection and Acoustic Absorptive Coating

Final Report

on EOARD GRANT No. FA9550-12-D-0003

Prepared by:

Alexander V. Fedorov and Vitaly G. Soudakov

Moscow Institute of Physics and Technology
Dolgoprudny, Moscow Region, Russia, 141700

January 2014

Abstract

This report summarizes results of stability analyses performed for a slender sharp cone with and without injection of air through a porous strip. The free-stream parameters are related to the experiments in the Caltech's T5 shock tunnel. The analysis is focused on pure aerodynamic effects in the framework of perfect gas model. It was shown that the injection leads to destabilization of acoustic modes in the near-field relaxation region. To reduce this detrimental effect it was suggested to alter the injector surface shape or use suction-blowing of zero net injection. However, stability computations showed that these modifications did not improve the injector performance. The porous wall effect on the acoustic instability was also examined. It was found that porosity stabilizes the boundary layer flow with and without injection. This indicates that the injector performance can be improved, if the porous layer, which is used for the injection, is protruded downstream to cover the near-field relaxation region.

Table of Contents

<i>Abstract</i>	1
<i>Table of Contents</i>	2
<i>Nomenclature</i>	3
<i>1. Introduction</i>	4
<i>2. Baseline configuration and numerical approach</i>	5
2.1 Results.....	7
<i>3. Shaping of the injector</i>	18
3.1 Conical injectors	20
3.2 Cylindrical injector	23
3.3 Cylindrical-conical injector	28
<i>4. Suction-blowing of zero total mass injection</i>	31
<i>5. Porous wall effect</i>	33
5.1 Porous coating for the baseline configuration	34
<i>6. Conclusions</i>	39
<i>References</i>	40

Nomenclature

A	acoustic admittance of a porous layer
a	local speed of sound
c	phase velocity
f	frequency
L	cone length along the symmetry axis
M	Mach number
\dot{m}	injection mass rate
N	amplification factor
P	mean-flow pressure
p	pressure
$q = \rho_w v_w$	mass flow rate of suction/blowing
\mathbf{q}	eigenfunction
Re	Reynolds number
T	temperature
T'	temperature disturbance
t	time
U	mean-flow velocity along the cone surface
(u, v, w)	velocity components of the disturbance
(x, y, z)	coordinates
α	streamwise component of the wavenumber vector
β	circumferential component of the wavenumber vector
δ	boundary-layer thickness
δ^*	displacement thickness
γ	specific heat ratio
ρ	density
σ	spatial growth rate
θ_c	half-angle of the cone
ϕ	porosity
ω	circular frequency
<i>Subscripts</i>	
a	sonic line
i	imaginary part
e	upper boundary-layer edge
r	real part
tr	transition onset
w	on the wall surface
∞	free-stream quantity
0	neutral point
<i>Superscripts</i>	
*	dimensional quantity

1. Introduction

It is well known that laminar-turbulent transition on slender bodies in a hypersonic flow at small angles of attack is caused by amplification of acoustic waves trapped in the boundary layer [1,2]. Non-equilibrium effects such as molecular vibrations and dissociation can damp acoustic disturbances [3,4]. Carbon dioxide has been found to be well suited to absorb acoustic energy in an enthalpy range relevant to realistic applications [5]. These findings point to the potential beneficial application of adding carbon dioxide into boundary-layer flows in order to delay transition onset. Experimentally, this is attempted by injecting CO₂ into the boundary layer through the wall.

In Ref. [6], three injection schemes were studied both as passive trips with no injection and as active trips with CO₂ injection. The first injector had four rows of 36 orifices. The second injector was derived from the former one by only keeping the fourth or most downstream row of orifices. The third injector consisted of a micro-porous section. It was found that the four-row injector tripped the boundary layer to fully turbulent values near the last row of orifices. The transition Reynolds number with the one-row injector was decreased by more than 50% as compared to the smooth cone. Therefore, while not as efficient as the four-row injector, one row of holes still caused early transition. A porous injector was also tested and did not result in early transition when tested without injection.

Due to the tendency of the discrete jets to cause transition, further studies were focused on the porous injector. The numerical simulations [7] predicted that transition should occur immediately following the injection of cold carbon dioxide. The test cases with air and nitrogen as the test gas suggested the momentum of the injection plays a dominant role in the amount of amplification seen immediately downstream due to the inefficient heating of the injected CO₂. To remedy this, the injected carbon dioxide was pre-heated, resulting in a reduction of amplification in the post-injection region. Despite this reduction, the stability analyses still predicted transition to occur earlier as compared to the case without injection. To isolate the effects of non-equilibrium processes on the disturbances, a second configuration involving a similar cone with a longer transpiration interval was investigated. For this case, the stability analyses predicted a window of carbon dioxide injection resulting in a reduction of amplification and thus a delay in transition. In Ref. [8], transition delays were documented in shots with CO₂ injection. The data showed a general trend of increasing delay with injection rate, before a sharp drop-off at the highest injection rate. However, the transition delay was essentially smaller than that observed in the free-stream with CO₂.

The foregoing studies indicate that the injector performance essentially depends on the balance between the stabilizing effect of carbon dioxide and the destabilizing effect of injection. The latter could be diminished by seeking for optimal distributions of the blow rate and/or shaping of the injection region. To reach this goal on economical basis, the following strategy was chosen: 1) Perform broad-band feasibility studies of different blowing configurations using the perfect gas model. 2) Select the most promising configurations and check their robustness by numerical modeling of CO₂ injection including non-equilibrium effects. 3) Design the CO₂ blowing system and test it in high-enthalpy shock tunnel.

This report is related to Step 1, where air is injected to the air flow and air is treated as a perfect gas. The analysis is focused on pure aerodynamic effects, i.e. absorption of acoustic energy by

CO₂ is not considered. It should be noted that the perfect-gas modeling is suitable for the near-filled region where the injected gas is relatively cold. Further downstream, where the injected gas is heated and it can effectively damp acoustic instabilities, the perfect gas model overestimates the disturbance growth rates and, thereby, under-predicts the injector efficiency.

The following cases are considered: A) Baseline configuration – a 5° half-angle sharp cone at zero angle of attack with the normal-wall blowing through a porous wall strip. This configuration is similar to that tested at Caltech’s T5 shock tunnel [6,8]. B) Baseline configuration with shaping of the injection region; C) Baseline configuration with the normal-wall suction and blowing of zero net injection. The free-stream parameters correspond to the run 2540 in the T5 shock tunnel, which was documented in Ref. [7]. For each case the laminar basic flow is computed using the in-house Navier-Stokes code HSFlow, and stability analyses are performed in the framework of linear stability theory (LST) using the in-house LST code. These tools were successfully exploited for stability and receptivity studies of high-speed boundary-layer flows [9-12].

Fedorov et al. [13] showed theoretically that a passive ultrasonically absorptive coating (UAC) may effectively stabilize the Mack second mode. Typical UAC constitutes a thin micro-porous layer, with average spacing between pores being much smaller than the boundary-layer thickness. The transition experiments of Rasheed et al. [14], which were performed on a sharp cone in the T5 shock tunnel, qualitatively agree with the theoretical predictions [13]. Further experimental, theoretical and numerical studies (see Rev. [2] and Ref. [15]) have demonstrated robustness of the UAC stabilization concept. This motivated us to analyze the UAC effect on the boundary layer instability in combination with the gas blowing. The analysis is performed using the LST computations with the impedance boundary conditions for disturbances on the porous wall. The UAC parameters are relevant to the porous injector tested in the T5 shock tunnel [6]. The UAC stabilization effect is evaluated for the baseline configuration A with and without injection.

2. Baseline configuration and numerical approach

As a first step, we consider the baseline configuration shown in Fig. 1. A 5° half-angle sharp cone has the region $128 \text{ mm} < x^* < 169 \text{ mm}$, where gas at the wall temperature is uniformly injected in the normal wall direction. In our computations, the total mass rate is ranged from zero to 13.5 g/s, where the upper limit approximately equals the double mass rate of the incoming boundary-layer flow.

The free-stream parameters correspond to the conditions of Run 2540 in the GALCIT T5 shock tunnel [7]: Mach number $M_\infty = 5.3$, static temperature $T_\infty^* = 1323.77 \text{ K}$, static pressure $p_\infty^* = 21993 \text{ Pa}$, density $\rho_\infty^* = 0.05788 \text{ kg/m}^3$, and wall temperature $T_w^* = 293 \text{ K}$. The cone length measured along the cone axis is $L^* = 1 \text{ m}$. The asterisks denote dimensional quantities. The Reynolds number based on the cone length is $\text{Re}_{\infty L} = 4.57 \cdot 10^6$.

Calculations of the mean flow are performed using the in-house Navier-Stokes code HSFlow for perfect gas of Prandtl number $\text{Pr} = 0.72$, specific heat ratio $\gamma = 1.4$ and Sutherland viscosity-temperature dependence, with the Sutherland constant being 110.4 K. The flow variables are made nondimensional using the free-stream parameters and the cone length $L^* = 1 \text{ m}$. Pressure

is scaled using the doubled free-stream dynamic pressure $\rho_{\infty}^* U_{\infty}^{*2}$, where U_{∞}^* is free-stream velocity.

The computational domain is a rectangle (Fig. 2). Its bottom boundary lies on the cone surface, and the upper boundary lies in the free stream above the cone-induced shock. The boundary conditions on the cone surface are the no-slip condition and the isothermal condition $T = T_w$. On the inflow and upper boundaries, the conditions correspond to the undisturbed free stream. On the outflow boundary, the unknown dependent variables are extrapolated using the linear approximation.

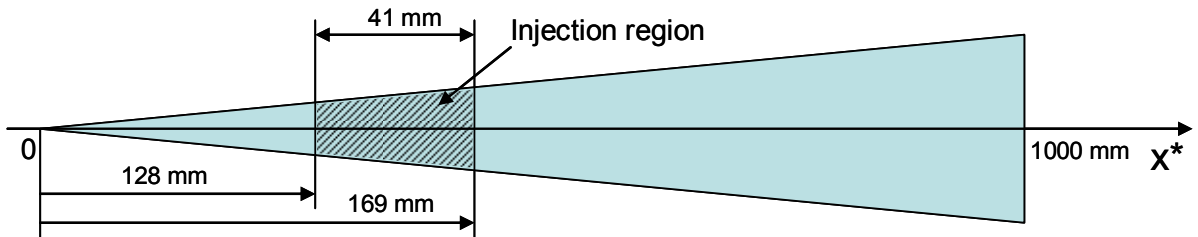


Figure 1 A 5° half-angle sharp cone with the injector – baseline configuration A.

The problem is solved numerically using the implicit second-order finite-volume method described in Ref. [9]. The two-dimensional (axisymmetric) Navier-Stokes equations are approximated by a shock-capturing scheme that allows for modeling of flow non-uniformities induced by the injector. The advection terms are approximated by the third-order WENO scheme [16] to decrease the numerical dissipation. The code algorithm as well as its implementations and validations are discussed in [9].

The grid convergence study showed that the basic laminar flow can be computed with sufficiently high accuracy using 597×649 grid. This grid is clustered in the direction normal to the cone surface so that the boundary-layer region contains approximately 50% of nodes. To resolve flow non-uniformities in the vicinity of injector, the grid is also clustered in the streamwise direction near the injector boundaries as shown in Fig. 3.

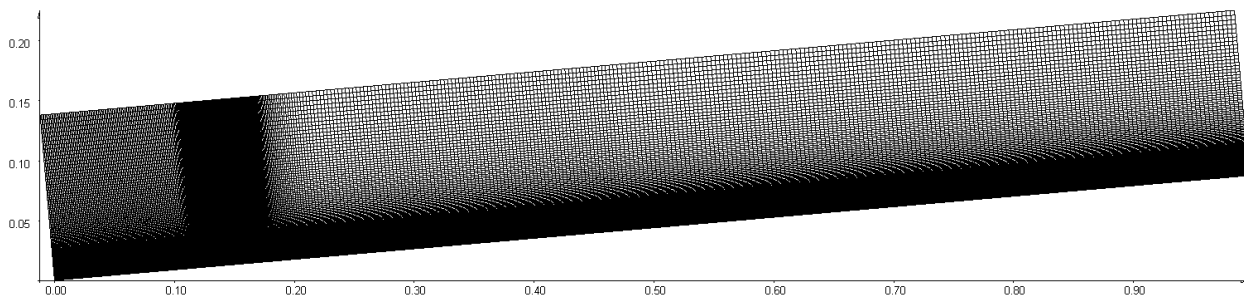


Figure 2 Computational domain and grid.

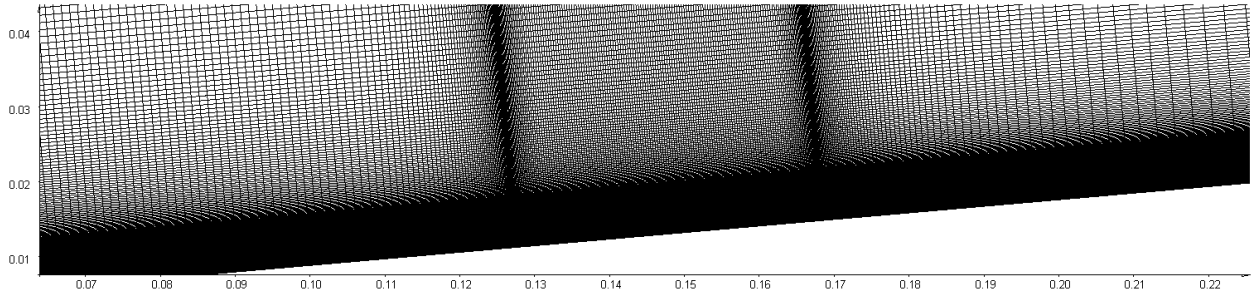


Figure 3 Close up view of the computational grid near the injector.

The mean flow profiles were used for the local-parallel stability analysis. The boundary-layer disturbance is considered in the wave form $\mathbf{q}(y) \exp(i\alpha x + i\beta z - i\omega t)$, where ω is angular frequency and α, β are streamwise and azimuthal components of the wavenumber vector, t is time. The vector \mathbf{q} consists of the eigenfunctions of velocity components u, v, w , pressure p and temperature T' . For each x -station the linear stability equations are solved using a 4th-order Runge-Kutta scheme and a Gram-Schmidt orthonormalization procedure. For the temporal stability problem, $\omega(\alpha, \beta, x)$ is a complex eigenvalue while α, β are real parameters. For the spatial stability problem, $\alpha(\omega, \beta, x)$ is a complex eigenvalue while β, ω are real parameters. The eigenvalues of discrete spectrum are calculated with the help of a shooting/Newton-Raphson procedure. The downstream amplification factors $N(x, \omega, \beta)$ are computed using solutions of the spatial stability problem

$$N(x, \omega, \beta) = \int_{x_0(\omega, \beta)}^x \sigma(\omega, \beta, x) dx, \quad (1)$$

where $\sigma = -\alpha_i$ is the spatial growth rate, and x_0 is the initial point, which can be the neutral point on the lower neutral branch or a certain fixed point. The subscript ‘ i ’ denotes the imaginary part of a complex quantity and ‘ r ’ denotes the real part.

2.1 Results

The mean flow fields of static pressure and radial velocity are shown in Figs. 4a,b for the case of injection with the total mass rate $\dot{m} = 13.5$ g/s (the corresponding nondimensional mass flow rate is $\rho_w v_w = 0.0181$). The close up views of axial velocity, static pressure and temperature fields in the injector vicinity are shown in Fig. 5, where the dashed lines indicate the injection boundaries. It is seen that the normal-wall blowing displaces the boundary layer and induces compression waves emanating from the upstream boundary of the injector. A cold dead-flow layer is formed near the wall. Its thickness is several times larger than the shear-layer thickness. Owing to the mixing process the dead-flow layer gets thinner and it is ultimately swallowed by the shear layer in the mid stations ($x \approx 0.6$). This trend is clearly seen in Fig. 6, where profiles of the streamwise velocity and temperature are shown for various x -stations. Figure 7 shows the

near-wall layer thickness $\delta(x)$ determined by the condition $U(\delta) = 0.99U_e$. After a sharp rise in the injection region, $\delta(x)$ decreases and slowly approaches the no-blow distribution. These CFD data demonstrate that the injection strongly affects the near-wall flow not only near the injector but also in a long post-injection region which is called hereafter as a relaxation region.

To get insight into stability of the near-wall layer with injection, we start with the temporal stability analysis for the mean flow profiles in the station $x = 0.298$ which lies in the middle of the relaxation region. The flow parameters are non-dimensionlized using their values at the upper edge of near-wall layer, the length scale is the displacement thickness δ^* and the time scale is δ^*/U_e^* . In the considered herein x -station, the local Mach number is $M_e \approx 5$ and the Reynolds number is $Re_{\delta^*} \approx 8074$.

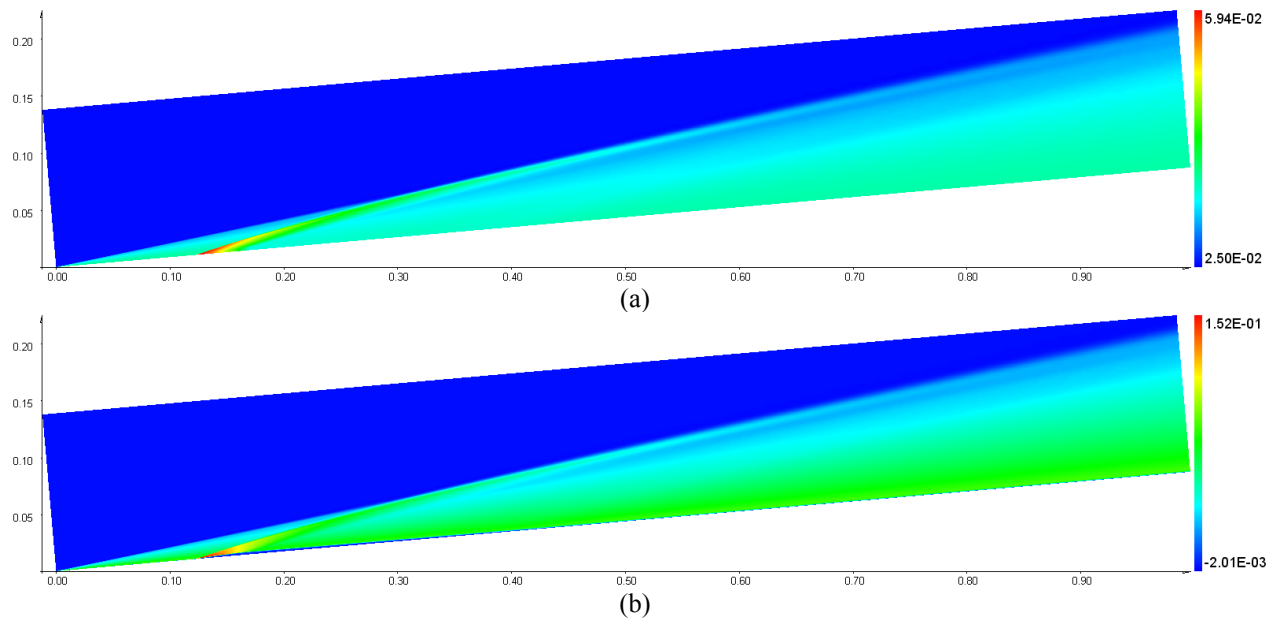


Figure 4 Basic flow fields for the static pressure (a), and radial velocity (b), the total mass rate $\dot{m} = 13.5$ g/s.

Using a global search for eigenvalues we found seven unstable modes whose increments $\omega_i(\alpha)$ and phase speeds $c_r(\alpha) = \omega_r(\alpha)/\alpha$ are plotted in Figs. 8 and 9. The computations were performed for plane waves of $\beta = 0$. Figure 10 shows the pressure eigenfunctions $p(y)$ for modes 0, 1, 2 and 3 with the wavenumbers α corresponding to maximal increments ω_i for each mode. The eigenfunction shapes indicate that we are dealing with trapped acoustic waves propagating in a waveguide formed between the wall and the relative sonic line $y = y_a : U(y_a) = c_r - a(y_a)$, where a is local speed of sound [2]. In the layer $0 < y < y_a$, where the mean flow is supersonic relative to the disturbance propagating with the phase velocity c_r , the eigenfunction $p_n(y)$ of mode n oscillates versus y so that the oscillation phase is approximately $\pi/4 + n\pi$, $n = 0, 1, \dots$. In the Mack terminology, mode with $n = 0$ corresponds to the second mode, mode with $n = 1$ – to the third mode etc. Because of relatively thick dead-

flow layer the wave guide is essentially thicker and the number of unstable acoustic modes is larger than in the no-blowing case.

It turned out that the phase speeds of acoustic instabilities are quite small compared with the no-blowing case. As shown in Fig. 11, the instabilities are observed in a wide range of c_r and their eigenvalues are close to the branches of slow acoustic waves of the continuous spectrum. The eigenfunctions of such slow modes oscillates outside the boundary layer with very weak damping (Fig. 12). This abnormal behavior may lead to a significant increase of receptivity to free-stream acoustic disturbances.

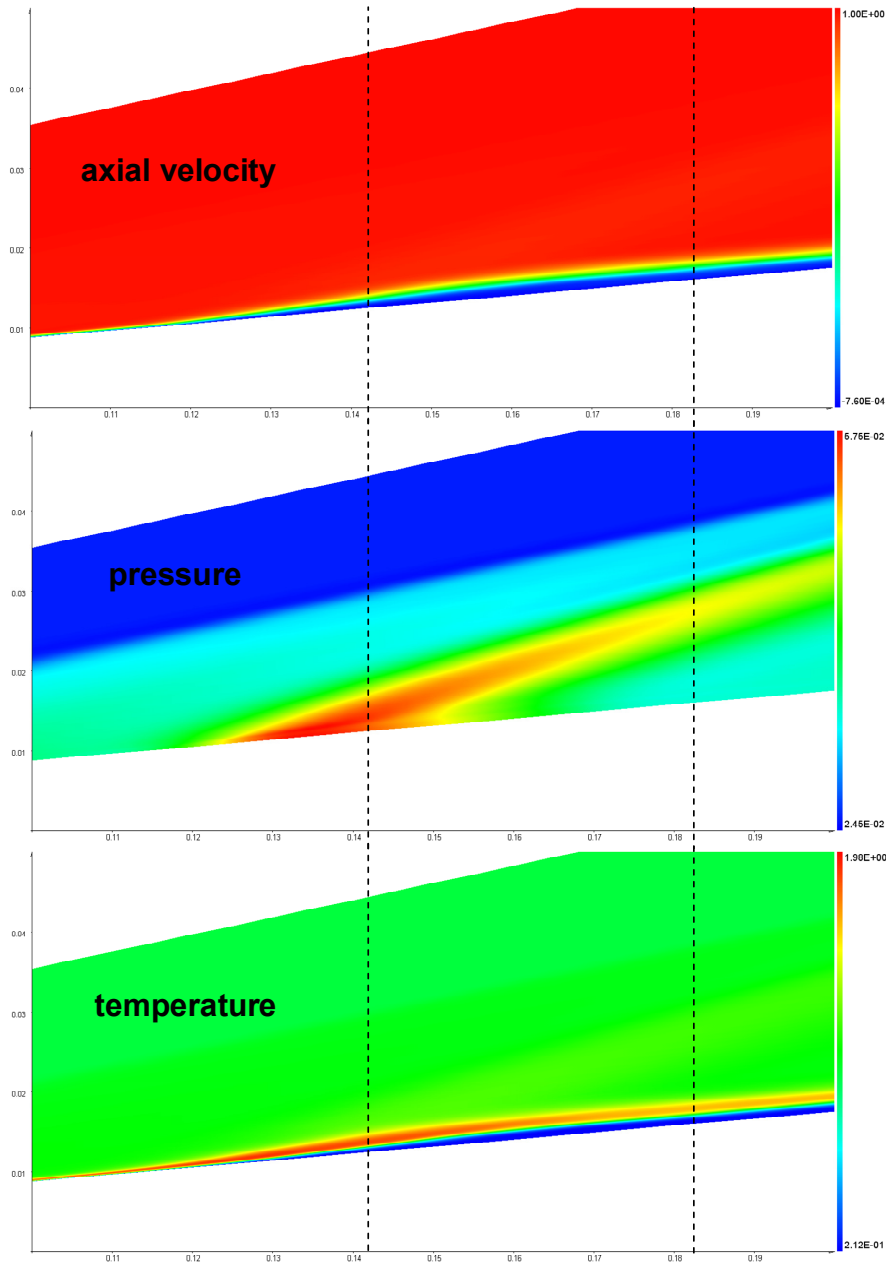
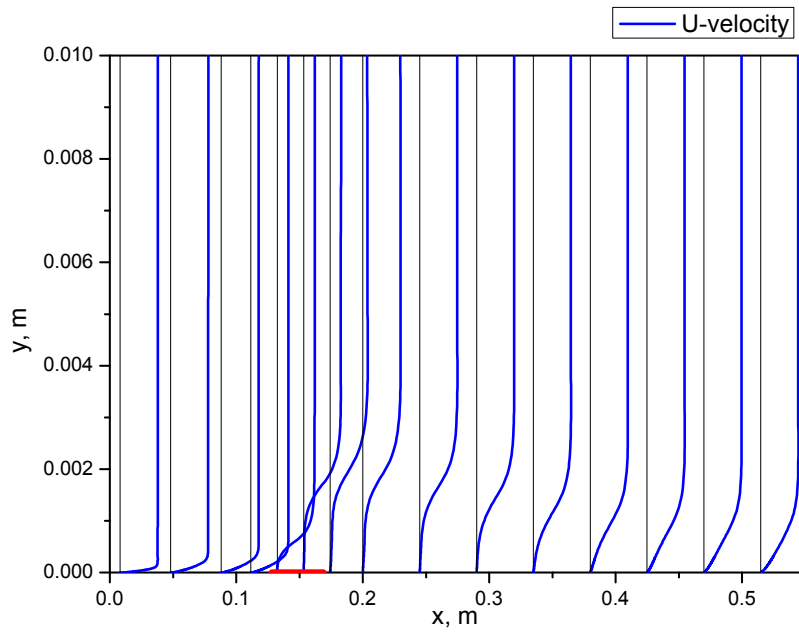
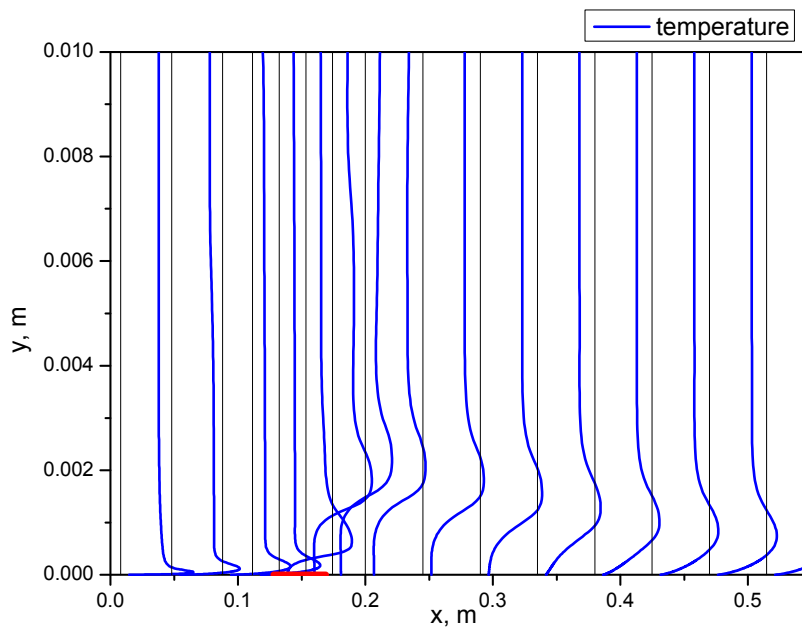


Figure 5 Basic flow fields for the axial velocity, pressure and temperature in the vicinity of injector, the total mass flow rate $\dot{m} = 13.5$ g/s. The dashed lines show the injection boundaries.



(a)



(b)

Figure 6 Profiles of the streamwise velocity $U(y)$ (a) and temperature $T(y)$ (b) at various x -stations, the total mass flow rate $\dot{m} = 13.5$ g/s, the injection region is shown by the red line.

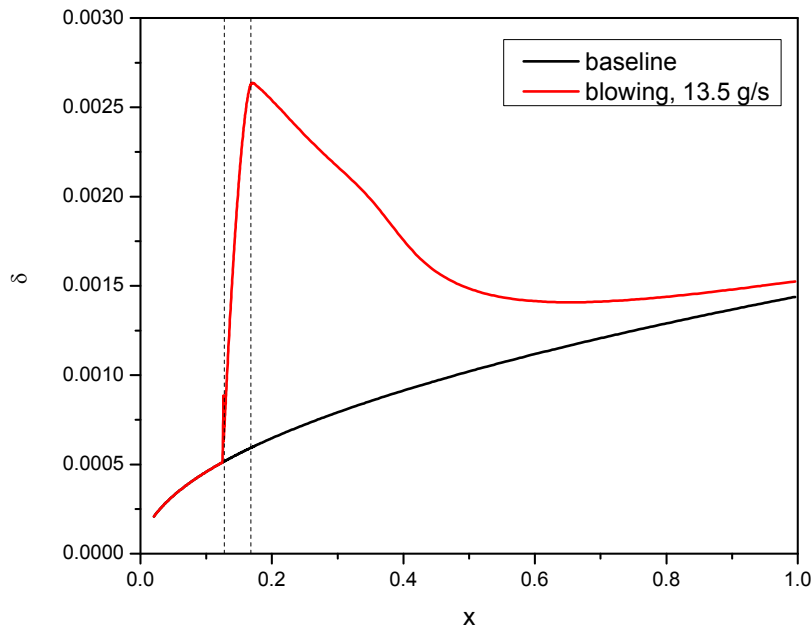


Figure 7 The boundary-layer thickness in the no-blow case (black line) and in the case of injection with $\dot{m} = 13.5$ g/s (red line).

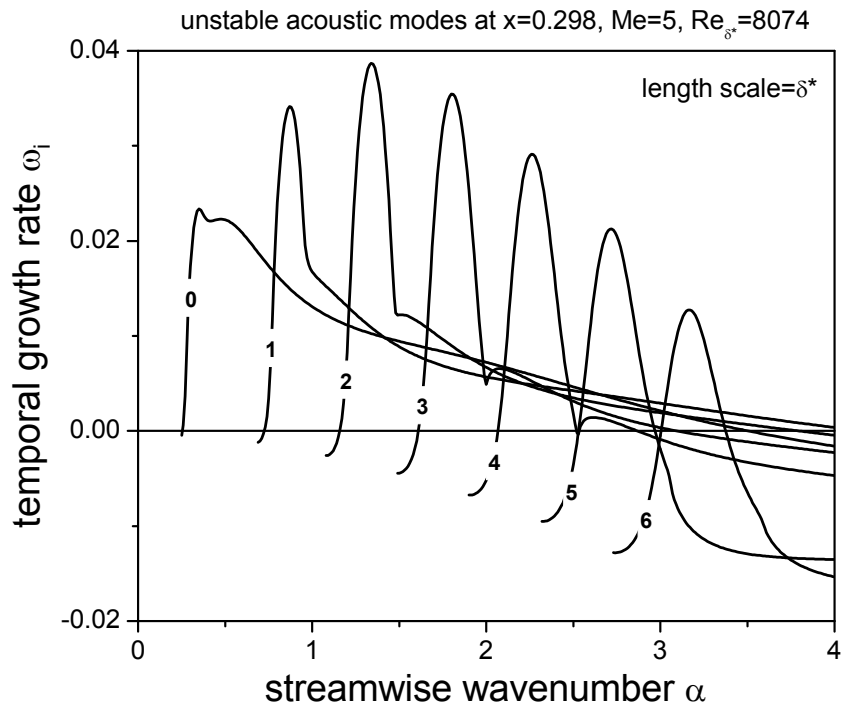


Figure 8 Growth rates $\omega_i(\alpha)$ of seven unstable modes at $x = 0.298$, $\beta = 0$.

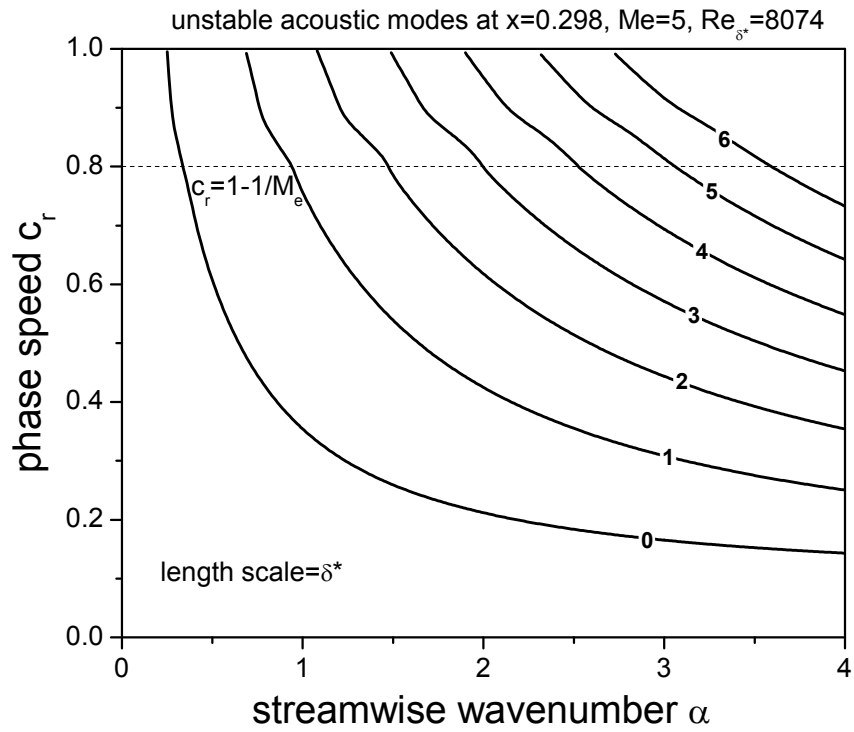
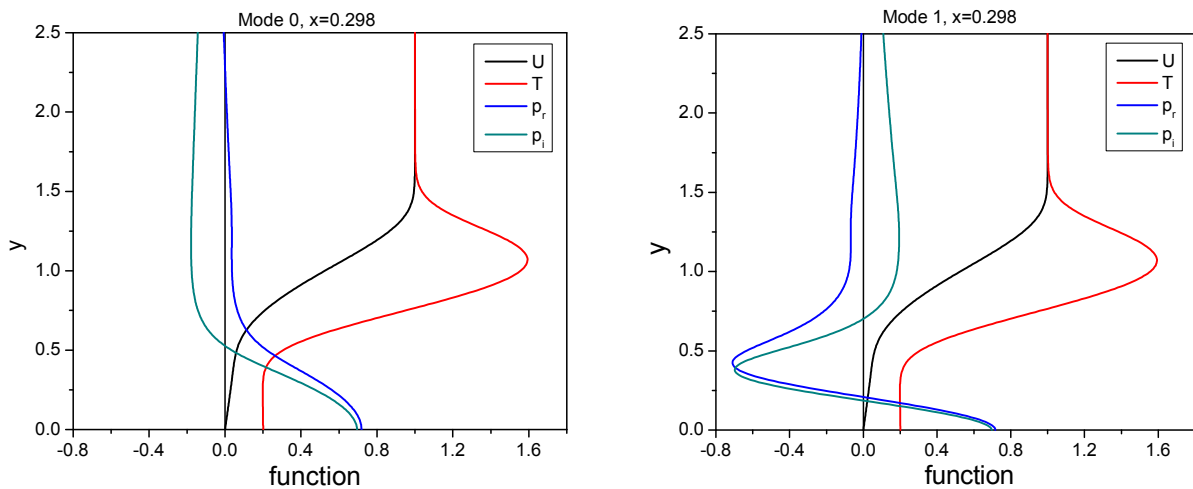


Figure 9 Phase speeds $c_r(\alpha)$ of seven unstable modes at $x = 0.298$, $\beta = 0$.



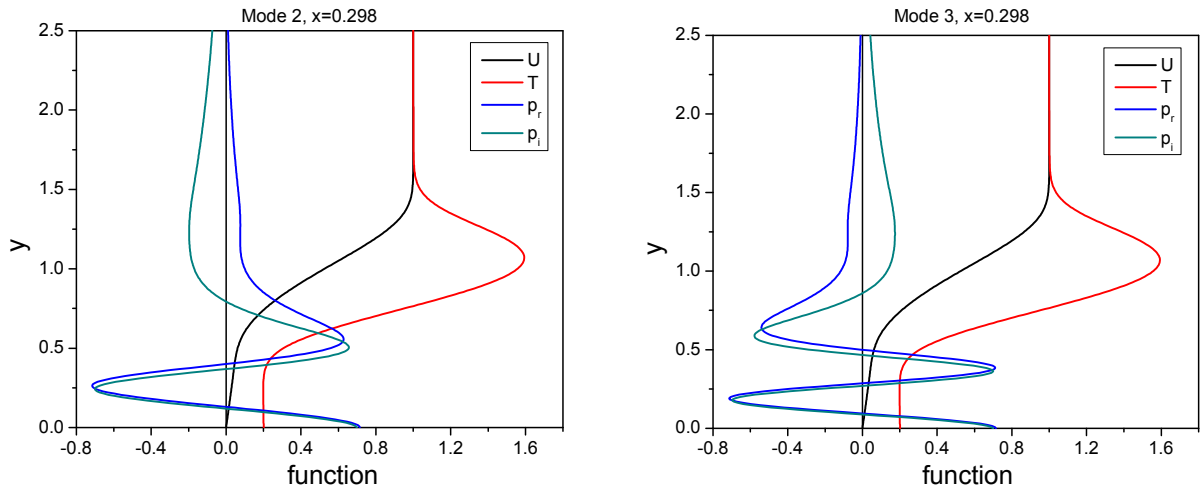


Figure 10 The pressure eigenfunctions $p_r(y)$ and $p_i(y)$ for modes 0, 1, 2 and 3 at (ω, α) corresponding maximal ω_i . The red and black lines show the mean flow profiles of streamwise velocity $U(y)$ and temperature $T(y)$, respectively.

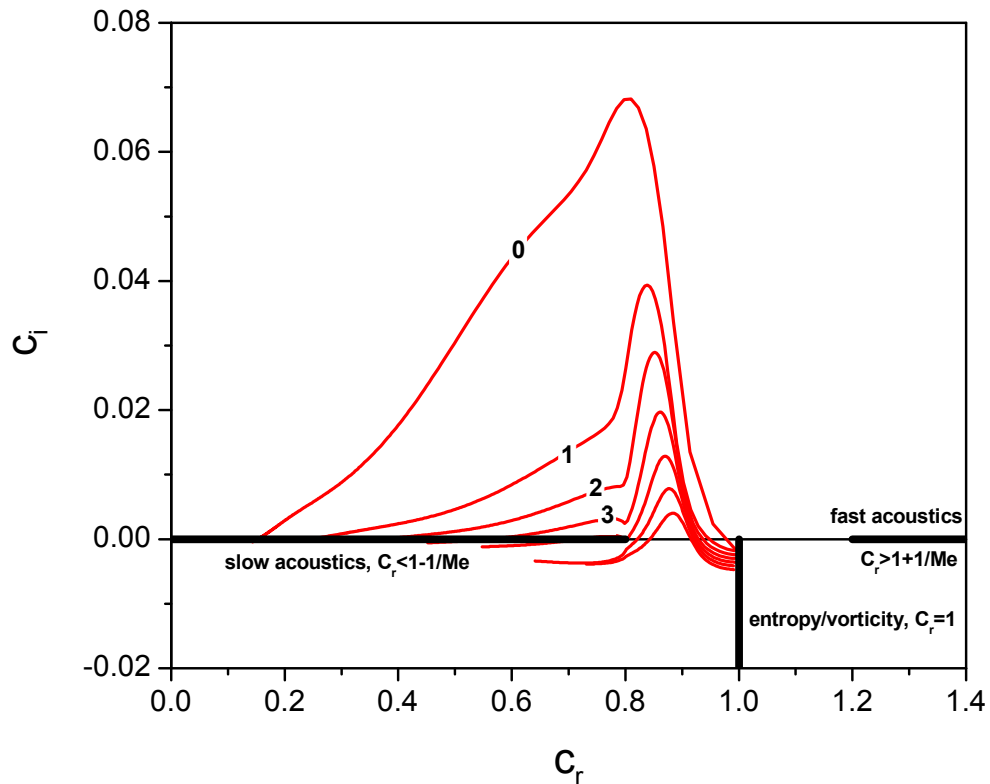


Figure 11 The phase speed trajectories (red lines) of unstable modes in the complex c plane, the branches of continuous spectrum are shown by the black lines.

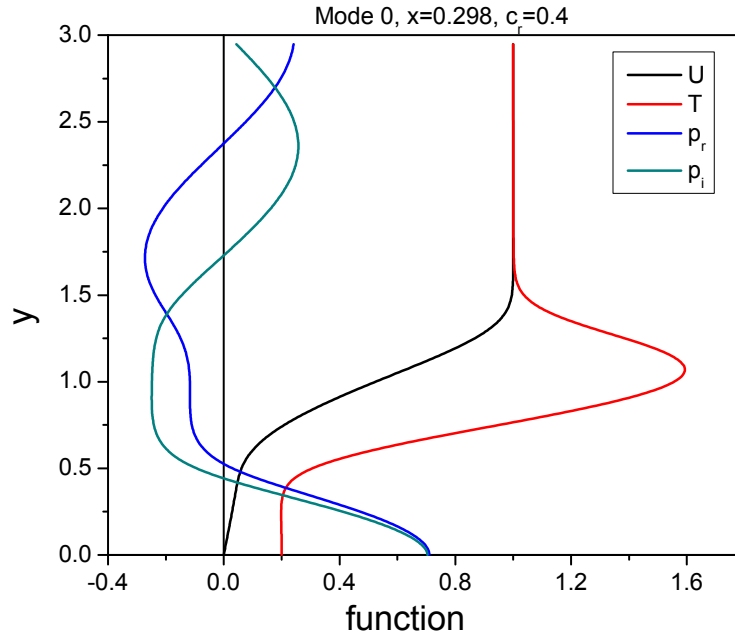


Figure 12 Eigenfunctions $p_r(y)$ and $p_i(y)$ of mode 0 (Mack second mode) at the phase speed $c_r = 0.4$. The red and black lines show the mean flow profiles of streamwise velocity $U(y)$ and temperature $T(y)$, respectively.

Note that maximal temporal instability corresponds to mode 2 which is the Mack fourth mode (Fig. 8). However the spatial stability analysis leads to the different conclusion. Figure 13 shows that the spatial growth rates $\sigma(\omega)$ are maximal for mode 0 corresponding to the Mack second mode – typical for hypersonic boundary-layer flows. This switch over is associated with abnormal behavior of the group velocities of the unstable modes considered.

Figure 14 shows distributions of maximal growth rates $\sigma_{\max}(x) = \max_{\omega} \sigma(\omega, x)$ for the five unstable modes in the relaxation region. In the all x -stations considered, the most unstable is mode 0. Computations for oblique waves ($\beta \neq 0$) showed that their growth rates are smaller than in the case of $\beta = 0$ – typical for acoustic instabilities. These findings allow us to restrict further parametric studies to the Mack second mode of $\beta = 0$, which is called hereafter as a Mack mode. It should be noted that the injection leads to significant destabilization of the Mack mode in a long region (compare the black and orange lines in Fig. 14).

Distributions of the Mack mode growth rates (upper panel) at various frequencies (lower panel) are shown in Fig. 15 for the no-blow case (blue lines) and the case with injection of $\dot{m} = 13.5$ g/s (black lines). The corresponding distributions of N-factors are shown in Fig. 16. As expected, the injection destabilizes the Mack mode in the relaxation region that gives a local maximum of the N-factor envelope at $x \approx 0.3$. Further downstream the maximal growth rates remain higher than in the no-blow case. However the width Δx of unstable regions is narrowed down that leads to decreasing of the integral amplification. As a result the N-factor envelope is lower than that of the no-blow case in the range $0.35 < x < 0.75$. In the far-field region $x > 0.6$ the mean flow is almost parallel and the growth rates weakly depend on x . This causes

a steep rise of the N-factor envelope. Eventually this envelope crosses that of no-blow case at $x \approx 0.75$.

The N factors for the case of $\dot{m} = 6.75$ g/s are shown by the red lines in Fig. 16. As expected, the near-field maximum of their envelope is significantly smaller than in the case of $\dot{m} = 13.5$ g/s. However, the relaxation region becomes shorter and the almost parallel mean flow sets in earlier. The envelope of steep slope is shifted upstream and the N-factors become larger than in the no-blowing and $\dot{m} = 13.5$ g/s cases for $x > 0.5$.

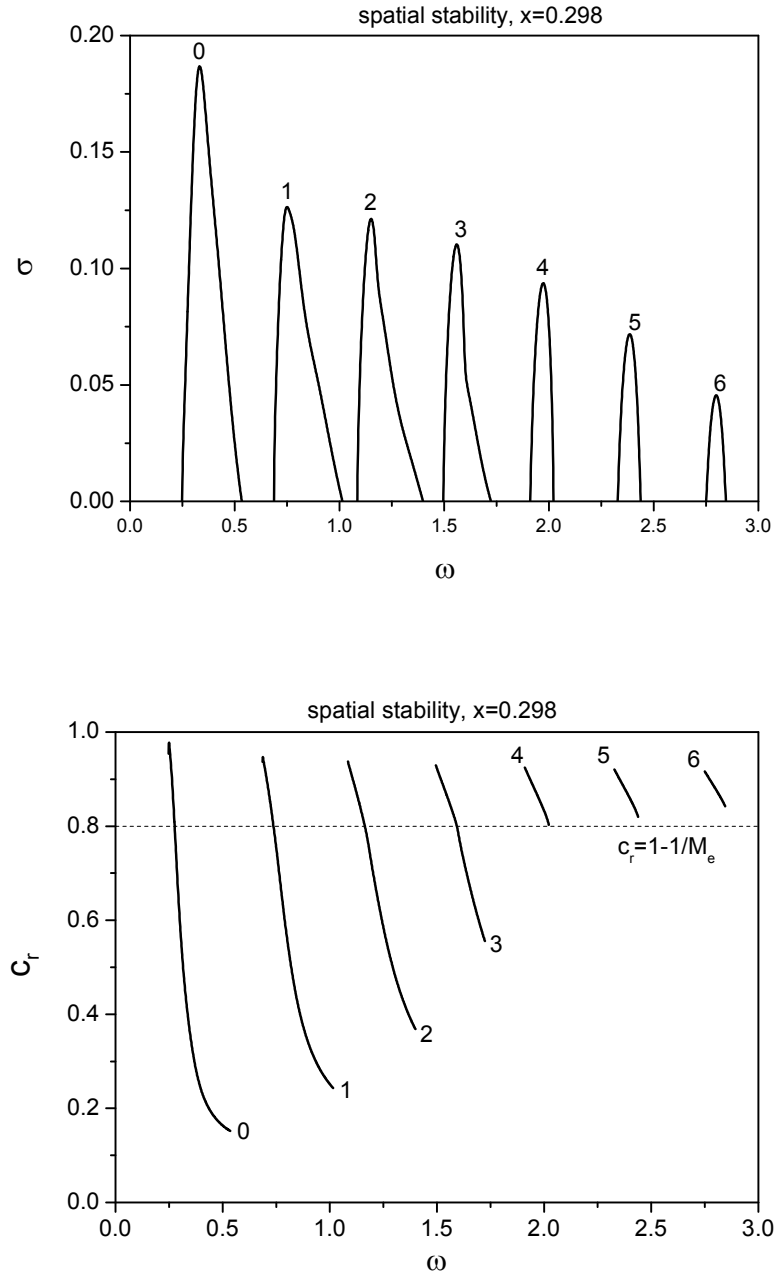


Figure 13 The growth rates $\sigma(\omega)$ and phase speeds $c_r(\omega)$ of seven unstable modes at $x = 0.298$, $\beta = 0$.

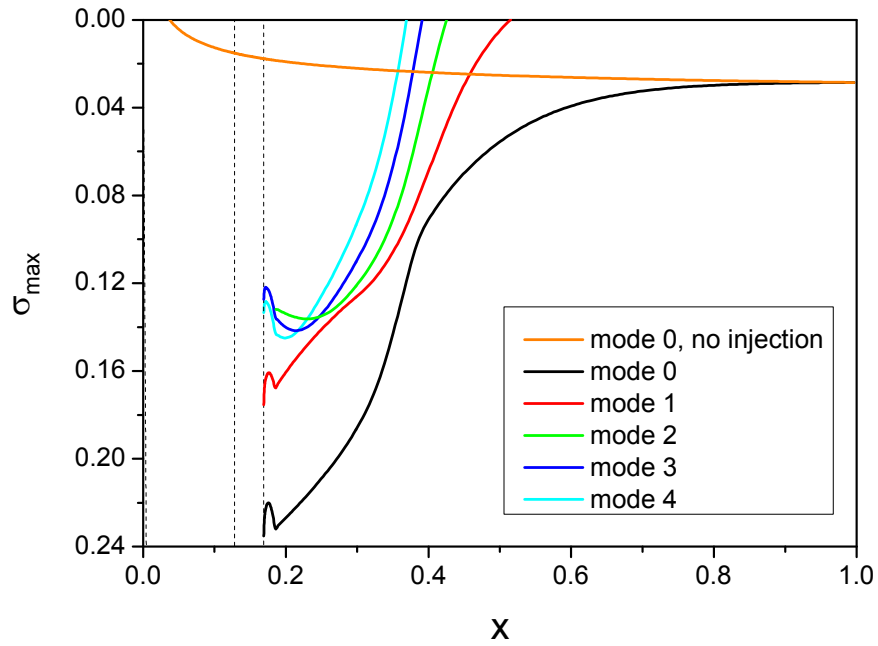
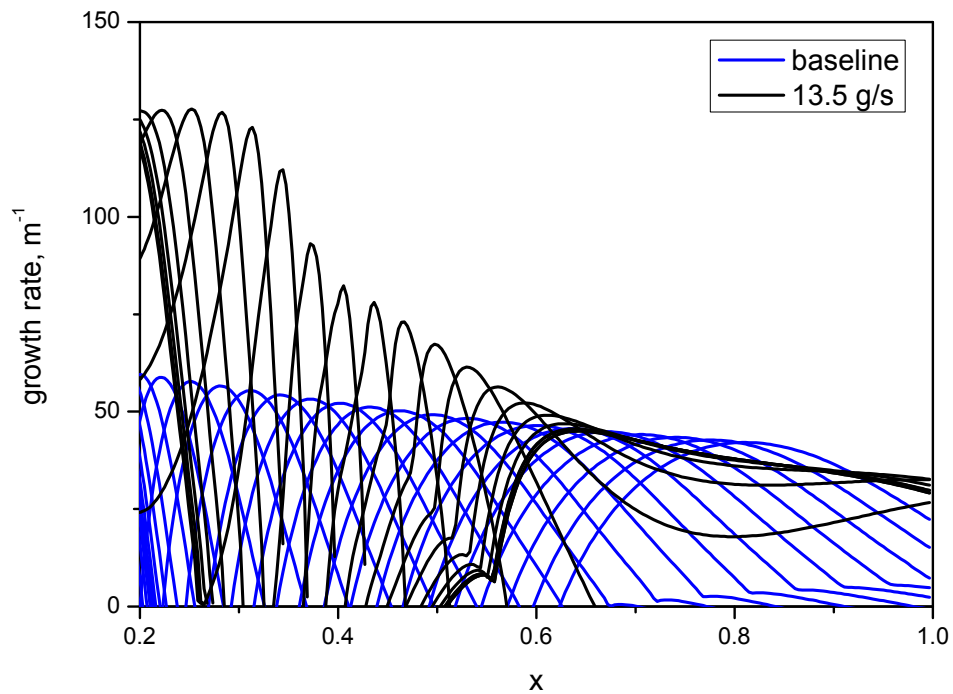


Figure 14 Distributions of maximal growth rates along the relaxation region in the case of injection with $\dot{m} = 13.5$ g/s; dashed lines show the injector boundaries; the orange line shows the baseline case without injection; $\beta = 0$.



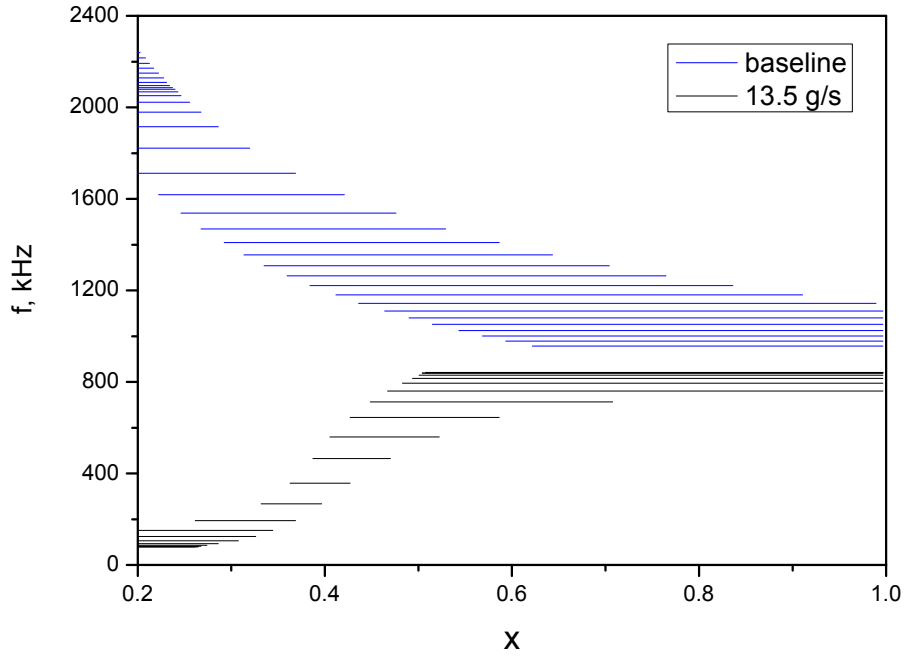


Figure 15 Growth rates and frequencies of the Mack mode for the no-blow case (blue lines) and the case with injection of $\dot{m} = 13.5$ g/s (black lines).

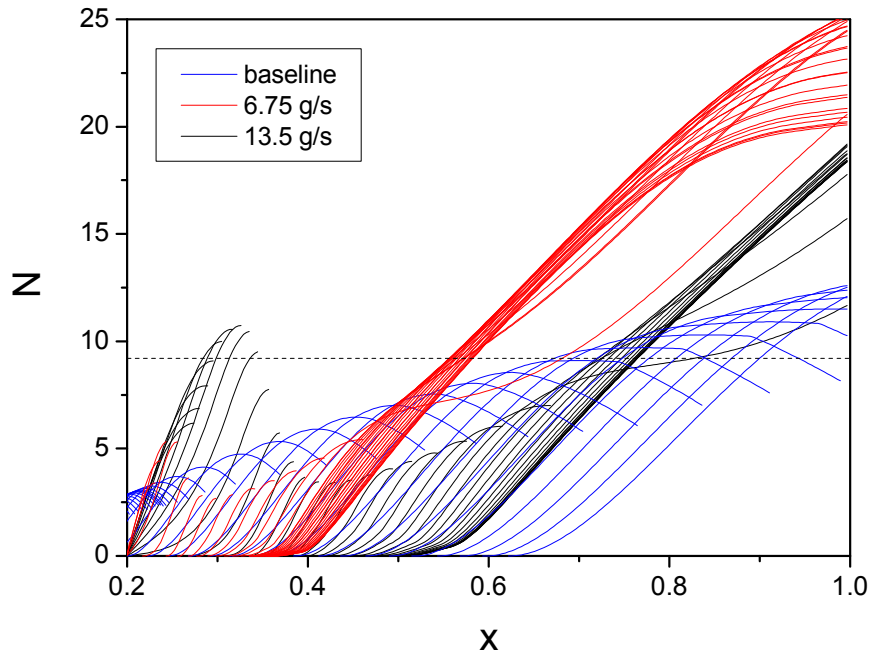


Figure 16 N-factors of the Mack mode for the no-blow case (blue lines), the case of $\dot{m} = 13.5$ g/s (black lines) and the case of $\dot{m} = 6.75$ g/s (red lines); dashed line – $N_{tr} = 9.2$.

Thus, the considered injection leads to destabilization of the near-field relaxation region, stabilization of the mid-field relaxation region, and destabilization of the far-field relaxation region where the basic flow is almost parallel. The width and location of these regions as well as the level of stabilization/destabilization effect depend on the injected mass rate. To estimate the transition onset we use hereafter the critical N-factor $N_{tr} = 9.2$, which has been derived in Ref. [7] from comparison of the e^N computations with the transition measurements on a 5 half-angle sharp cone without injector, which was tested in the GALCIT T5 shock tunnel. For sufficiently large \dot{m} , at which the maximum of N-factor envelope N_{max} in the near-filed relaxation region is higher than the critical $N = N_{tr}$, the transition onset point x_{tr} is predicted to be close to the injector. Decreasing of \dot{m} weakly affects x_{tr} until N_{max} becomes lower than N_{tr} . At this moment the transition point jumps to the x -station, which may be even downstream from the transition point in the no-blowing case; i.e., the premature tripping may be switched to delay in transition. Further decreasing of \dot{m} to a certain level can move the transition point upstream. Note that the data in Fig. 16 are consistent with those of Ref. [7] where stability computations were performed for CO₂ injection including real-gas effects. This convinces us that the perfect gas modeling can be used for a first-cut evaluation of the injector performance.

3. Shaping of the injector

The foregoing stability analysis suggests that the injector performance may be improved by shaping of the injection region. It was suspected that decreasing of the injector surface slope can partially compensate the displacement effect induced by the blowing and, presumably, reduce the instability growth in the relaxation region. This speculation was examined by parametric stability studies of the following configurations.

The first configuration is schematically shown in Fig. 17. The injection region has a conical shape. The rear part of the original cone ($x > 169$ mm) is shifted along the x -axis to Δb , and it is connected with the fore part through a conical surface (red line) used for injection. The angle of the new injector surface decreases from $\theta_c = 5^\circ$ to $\theta_c - \Delta\theta$ and its x -length increases from $b = 41$ mm to $b + \Delta b$. For this configuration stability computations were performed for the injector shapes corresponding to $\Delta\theta = 1^\circ$ and 3° . The total mass flow rates were $\dot{m} = 0, 6.75$ and 13.5 g/s for each shape.

The second configuration has the injector of cylindrical shape shown in Fig. 18. In this case $\Delta\theta = 5^\circ$ and the injector length is 41 mm. Stability computations were performed at $\dot{m} = 0, 1.35, 4.05, 6.75, 9.45$ and 13.5 g/s.

The third configuration is a combination of cylindrical and conical parts shown in Fig. 19. These parts of the injector surface are connected at the mid point $(x_1 + x_2)/2$. Stability computations are performed at $\dot{m} = 13.5$ g/s.

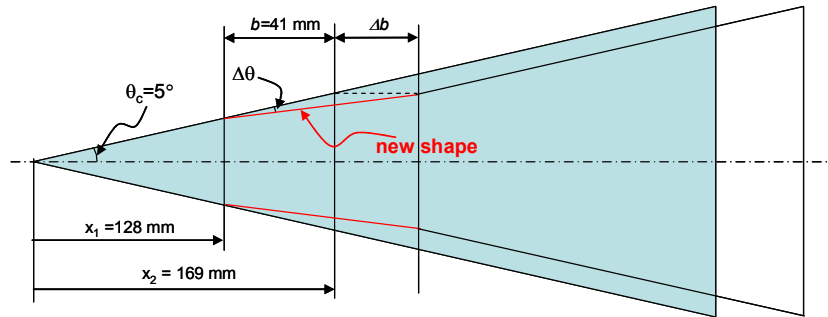


Figure 17 Injector of conical shape.

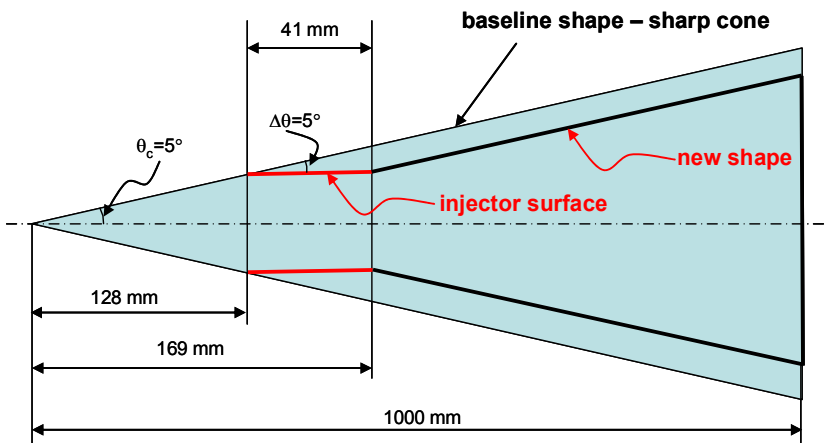


Figure 18 Injector of cylindrical shape.

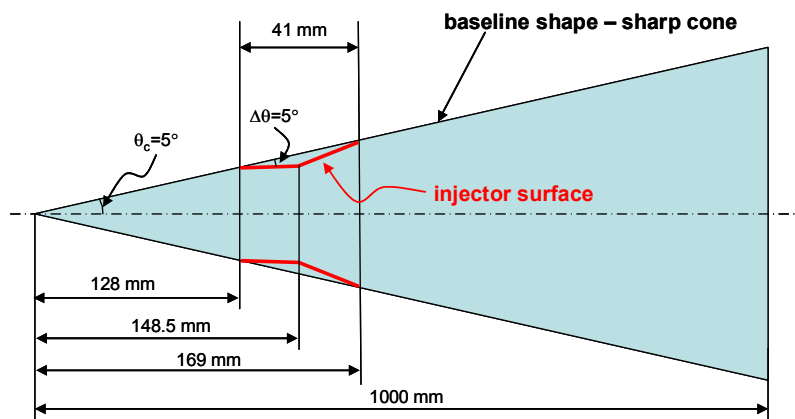


Figure 19 Injector of cylindrical-conical shape.

3.1 Conical injectors

Stability computations for the conical injector shapes of $\Delta\theta = 1^\circ$ and 3° at zero blowing showed that the shaping weakly affect N factors of the Mack mode. As an example, Figure 20 compares the distributions $N(x)$ for the baseline case (straight cone) with the case of $\Delta\theta = 3^\circ$. The corresponding distributions of the boundary-layer thickness (Fig. 21) indicate that the shaping without blowing produces a local effect on the mean flow. For $x > 0.2$ and $x < 0.128$, the distributions are close to each other.

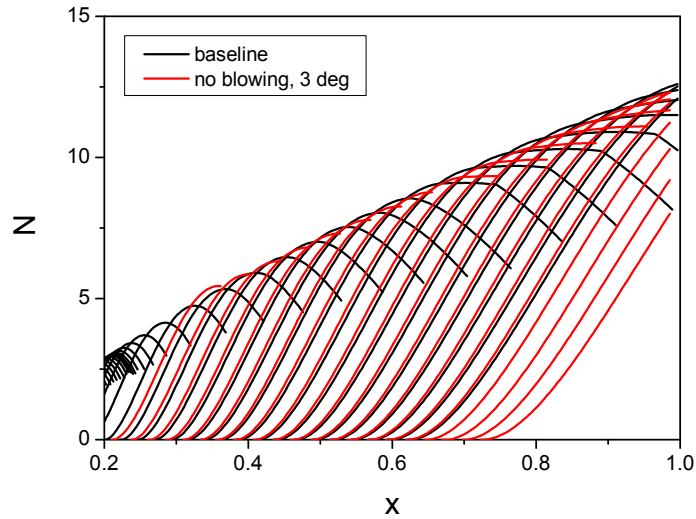


Figure 20 N-factors of the Mack mode for the straight cone (black lines) and for the shape of $\Delta\theta = 3^\circ$ (red lines) at $\dot{m} = 0$ g/s.

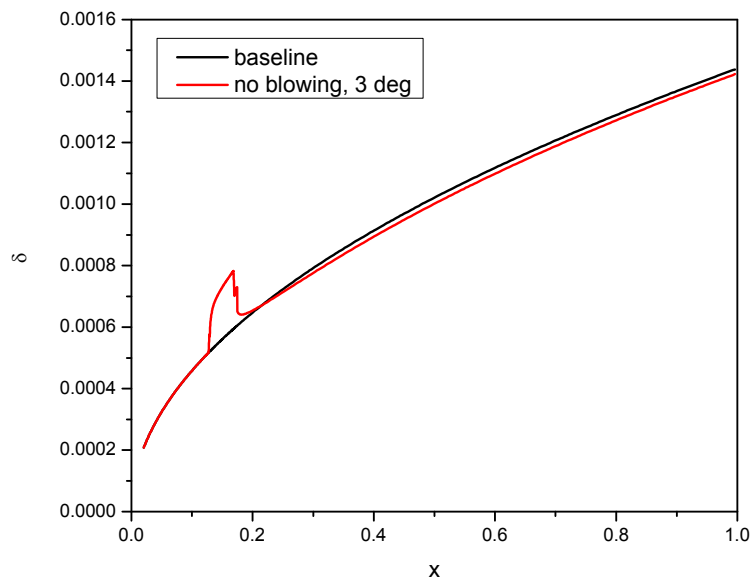


Figure 21 The boundary-layer thickness for the straight cone (black line) and for the shape of $\Delta\theta = 3^\circ$ (red line) at $\dot{m} = 0$ g/s.

Now we consider the conical injectors of $\Delta\theta = 0^\circ$, 1° and 3° at the fixed mass flow rate $\dot{m} = 13.5$ g/s. Figures 22 and 23 compare the basic flow fields for static pressure and axial velocity, respectively. As expected, the injector shaping reduces the pressure perturbations induced by the boundary-layer displacement. However, the thickness of dead-flow layer and, as a consequence, the length of relaxation region increase with $\Delta\theta$ (see distributions of $\delta(x)$ in Fig. 24).

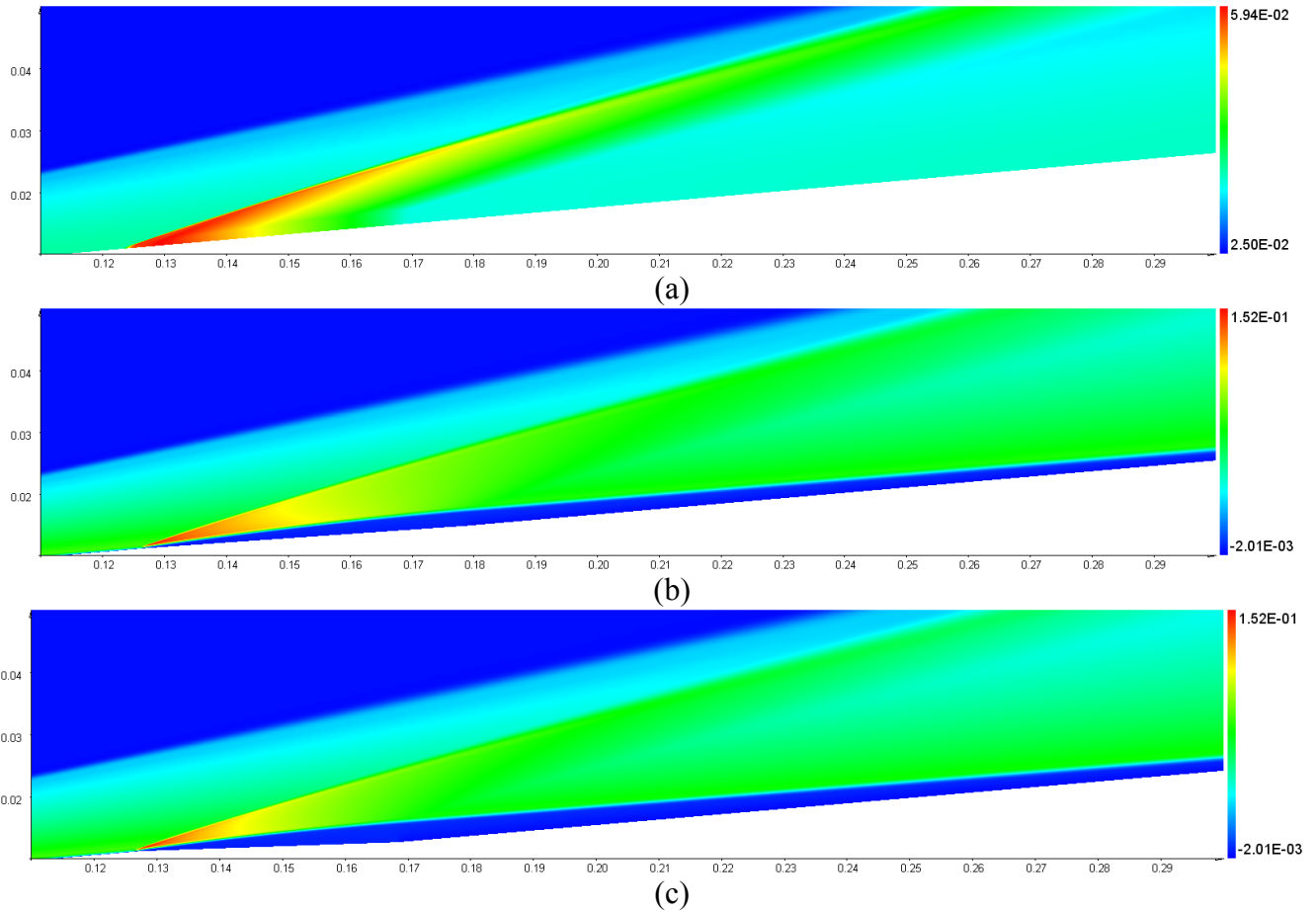
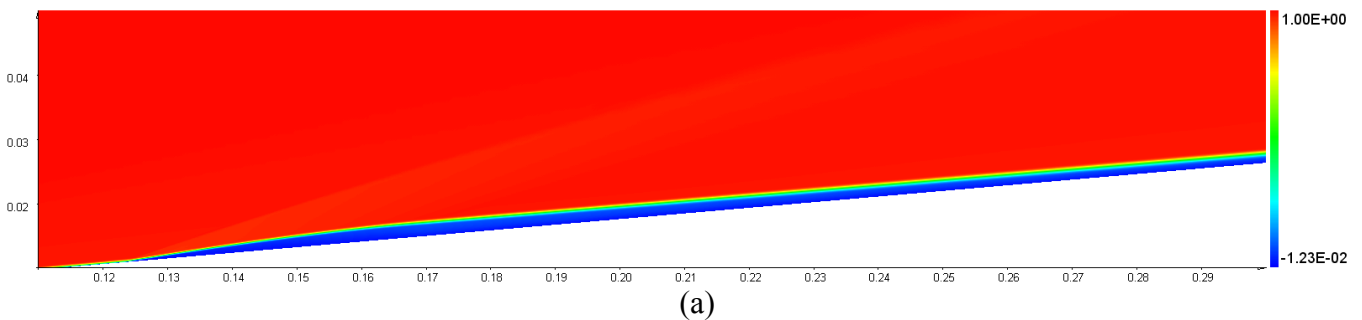


Figure 22 Mean flow fields for the static pressure at the total mass flow rate $\dot{m} = 13.5$ g/s; (a) – $\Delta\theta = 0^\circ$ (cone), (b) – $\Delta\theta = 1^\circ$, (c) – $\Delta\theta = 3^\circ$.



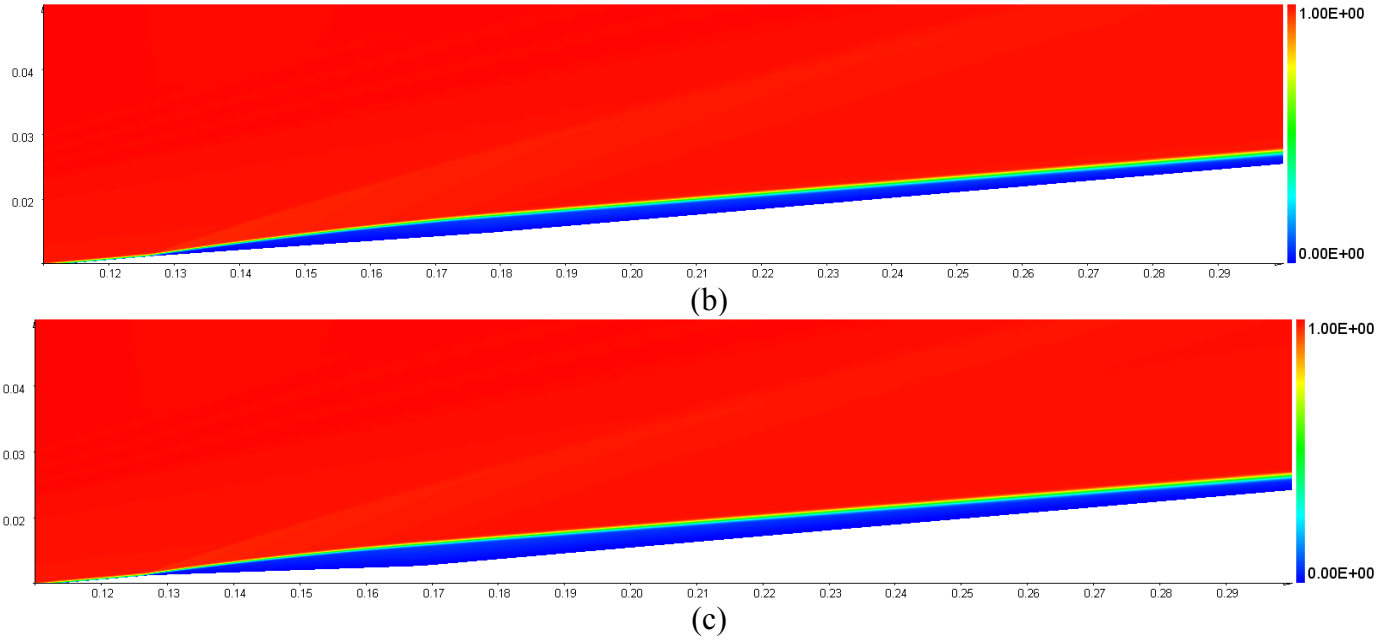


Figure 23 Mean flow fields for the axial velocity at the total mass flow rate $\dot{m} = 13.5$ g/s; (a) – $\Delta\theta = 0^\circ$ (cone), (b) – $\Delta\theta = 1^\circ$, (c) – $\Delta\theta = 3^\circ$.

Figure 25 shows the N factors computed for the mean flows presented in Figs. 22 and 23. It is seen that the injector shaping produces a weak destabilization effect in the near-field relaxation region $0.2 < x < 0.4$ and a noticeable stabilization effect in the mid-field and far-field relaxation regions. Because the near-field maximum of the N-factor envelope remains to be higher than the critical level N_{tr} , these injectors may cause premature transition at $x \approx 0.25$.

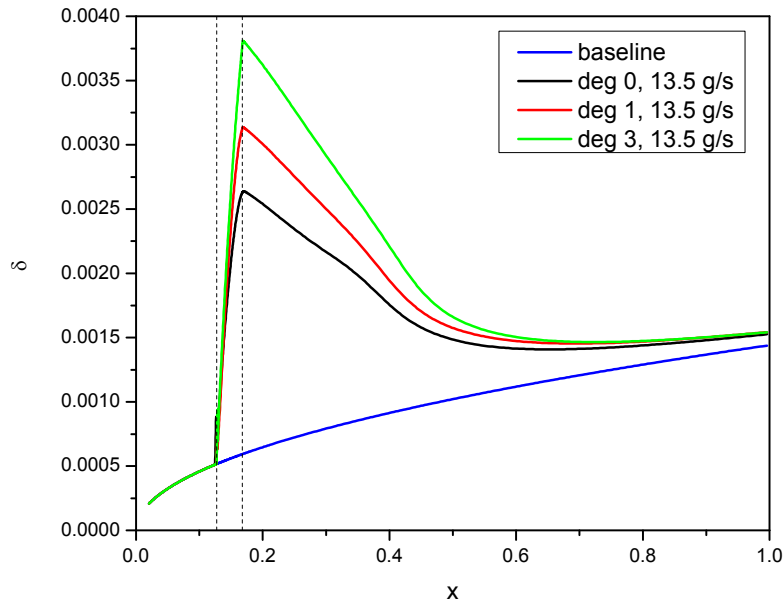


Figure 24 Distributions of the boundary-layer thickness at $\Delta\theta = 0^\circ$ (cone), $\Delta\theta = 1^\circ$ and $\Delta\theta = 3^\circ$. The total mass flow rate is $\dot{m} = 13.5$ g/s.

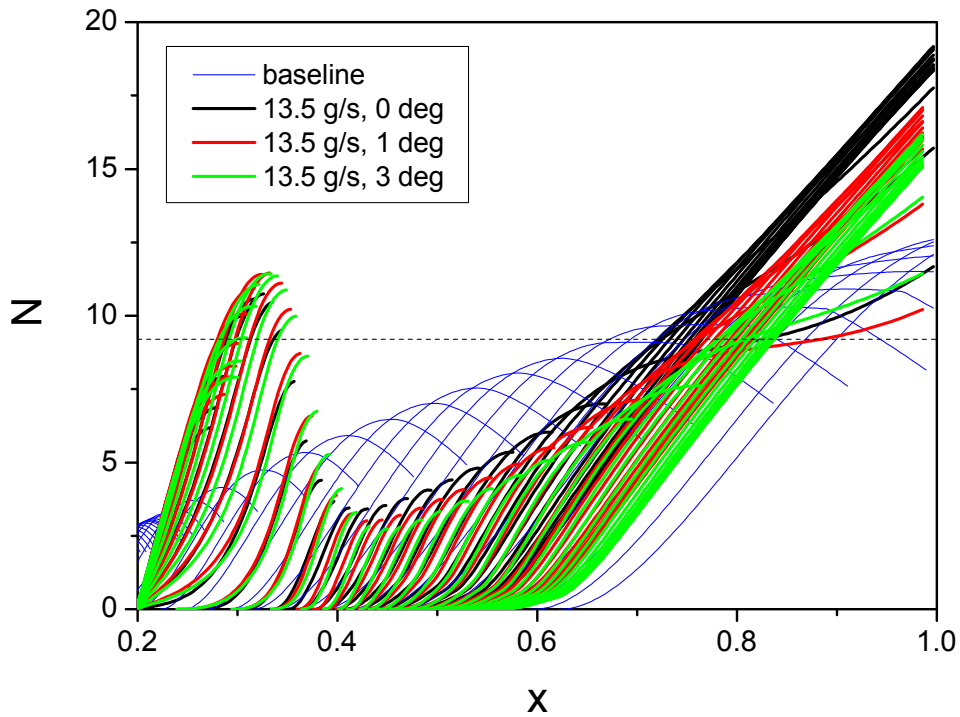


Figure 25 N-factors of the Mack mode for the straight cone with zero blowing (blue lines, baseline case), and for injectors of $\Delta\theta = 0^\circ$ (black lines), $\Delta\theta = 1^\circ$ (red lines) and $\Delta\theta = 3^\circ$ (green lines) at $\dot{m} = 13.5$ g/s; dashed line – $N_{tr} = 9.2$.

3.2 Cylindrical injector

Consider the cylindrical injector depicted in Fig. 18. Close up views of the pressure and axial velocity fields are shown in Figs. 26 and 27 for the case of $\dot{m} = 13.5$ g/s. Comparing these fields with the baseline case (Figs. 22 and 23) we conclude that the shaping reduces the pressure wave induced by the blowing – consistent with the original expectation. The dead-flow region, however, becomes essentially thicker.

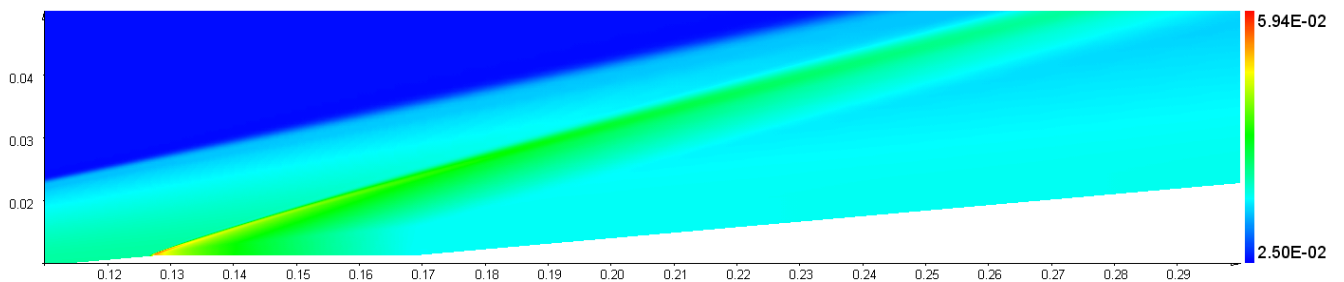


Figure 26 Static pressure near the injector of $\Delta\theta = 5^\circ$, $0.11 < x < 0.3$, $\dot{m} = 13.5$ g/s.

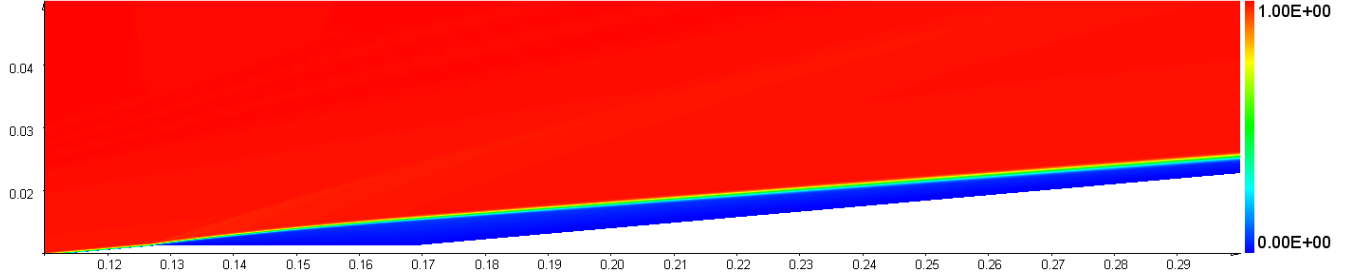


Figure 27 Axial velocity near the injector of $\Delta\theta = 5^\circ$, $0.11 < x < 0.3$, $\dot{m} = 13.5$ g/s.

Figure 28 shows the wall-pressure distributions $P_w(x)$ of the mean flow for different injection rates \dot{m} from 0 to 13.5 g/s. The dashed lines correspond to the injection boundaries. For a straight cone without injection the baseline distribution is approximately uniform (the solid black line). The shaping without blowing (the red line) leads to the pressure drop on the injector surface. This behavior is consistent with the slender body theory for inviscid flows. The blowing causes a sharp increase of P_w near the upstream boundary of the injector. Then P_w decreases to the level, which is lower than in the baseline case. Further downstream (in the relaxation region) the wall pressure is almost constant. The length of P_w plateau increases while its level decreases as the injection mass flow rate increases.

Figure 29 shows the corresponding distributions of the boundary-layer thickness $\delta(x)$. In the no-blowing case, the shaping effect is local and relatively weak. As the injection rate increases, the boundary-layer thickness quickly increases in the injection region. Its maximum at $\dot{m} = 13.5$ g/s is an order of magnitude larger than in the baseline case. Further downstream the boundary-layer thickness slowly decreases approaching the unperturbed (baseline) distribution.

These mean-flow changes affect the maximal (vs. frequency) growth rates of the Mack mode as shown in Fig. 30. The shaping itself (red line for the case of $\dot{m} = 0$) weakly influences on the distribution of σ_{\max} . As \dot{m} increases, a sharp peak of $\sigma_{\max}(x)$ is formed near the upstream boundary of injection $x \approx 0.13$. Another maximum is observed in the relaxation region. Because its location is shifted downstream with \dot{m} , the injection affects the N-factor distributions in a nontrivial manner (Fig. 31). The first maximum of the N-factor envelope (which is located in the near-field relaxation region) increases with \dot{m} , while the region of steep envelope (which is located in the far-field relaxation region) is shifted downstream. Because the N-factor envelopes are non-monotonic vs. x , the e^N method predicts different transition onsets depending on the choice of critical N . For $N_{tr} = 9.2$ (horizontal dashed line), the most promising cases are related to the injection with $\dot{m} = 6.75 - 9.45$ g/s.

Figure 32 compares the N-factors for the cases of $\Delta\theta = 0^\circ$ (cone without shaping) and $\Delta\theta = 5^\circ$ (cylindrical injector) at $\dot{m} = 6.75$ g/s and 13.5 g/s, respectively. Although the cylindrical injector works better in the mid-field and far-field relaxation regions, its performance is not improved in the most critical near-field region where the N factor envelope has a local maximum.

Thus, the e^N analysis indicates that the considered herein shaping does not prevent from early transition in the near-field relaxation region at sufficiently large injection rates (e.g., the lower panel in Fig. 32). For moderate \dot{m} , at which N-factors in the near-field region are below the

critical level (e.g., the upper panel in Fig. 32), the shaping produces a significant stabilization effect in the mid-field and far-field relaxation regions.

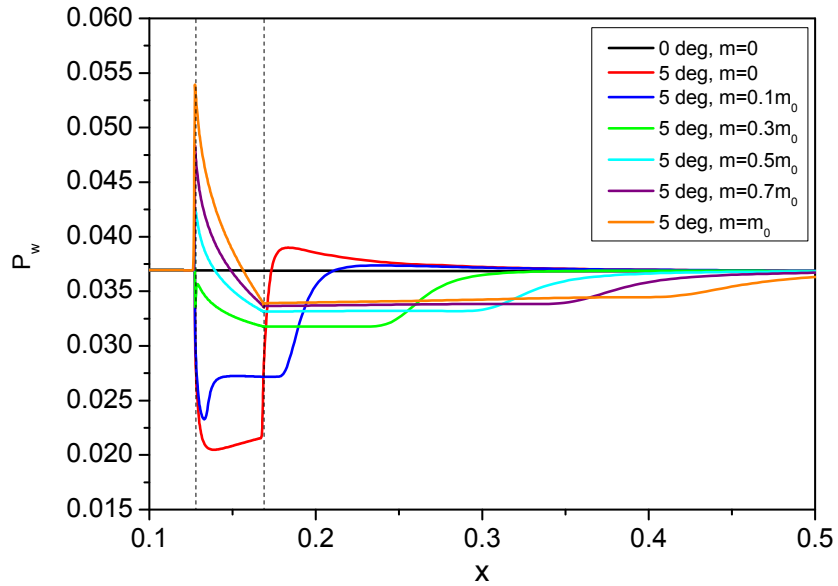


Figure 28 The mean-flow wall-pressure distributions in the region $0.1 \leq x \leq 0.5$ at the total mass rate from 0 to 13.5 g/s; dashed lines show the injection boundaries.

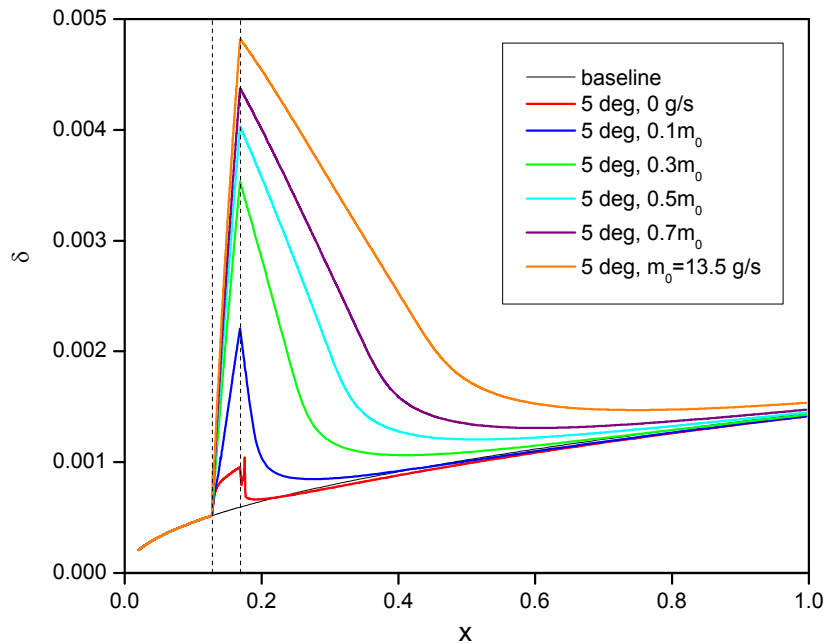


Figure 29 Distributions of the boundary-layer thickness at the total mass rate from 0 to 13.5 g/s; the cylindrical injector of $\Delta\theta = 5^\circ$.

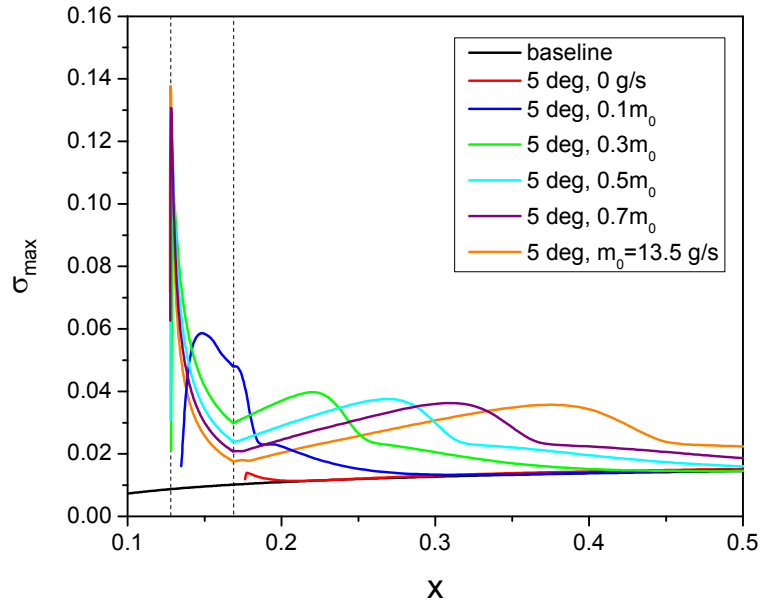


Figure 30 Maximal (vs. frequency) growth rates of the Mack mode. Black line – baseline case of straight cone without injection. Colored lines – cylindrical injector ($\Delta\theta = 5^\circ$) with different mass flow rates from 0 to $\dot{m}_0 = 13.5$ g/s. Dashed lines show the boundaries of injection. σ_{max} is made nondimensional using the Blasius length scale $\sqrt{\nu_e^* x^* / U_e^*}$.

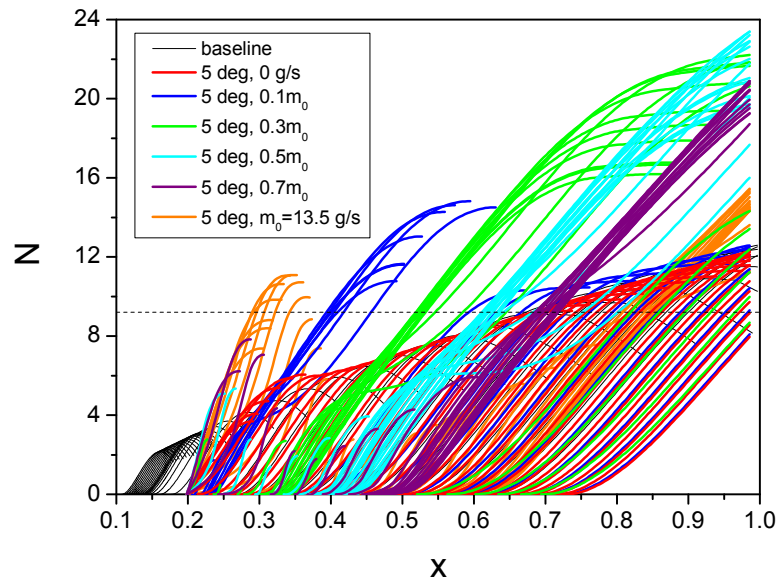


Figure 31 N-factors of the Mack mode for the cylindrical injector ($\Delta\theta = 5^\circ$) at different injection mass flow rates from 0 g/s to $\dot{m}_0 = 13.5$ g/s; dashed line – $N_{tr} = 9.2$.

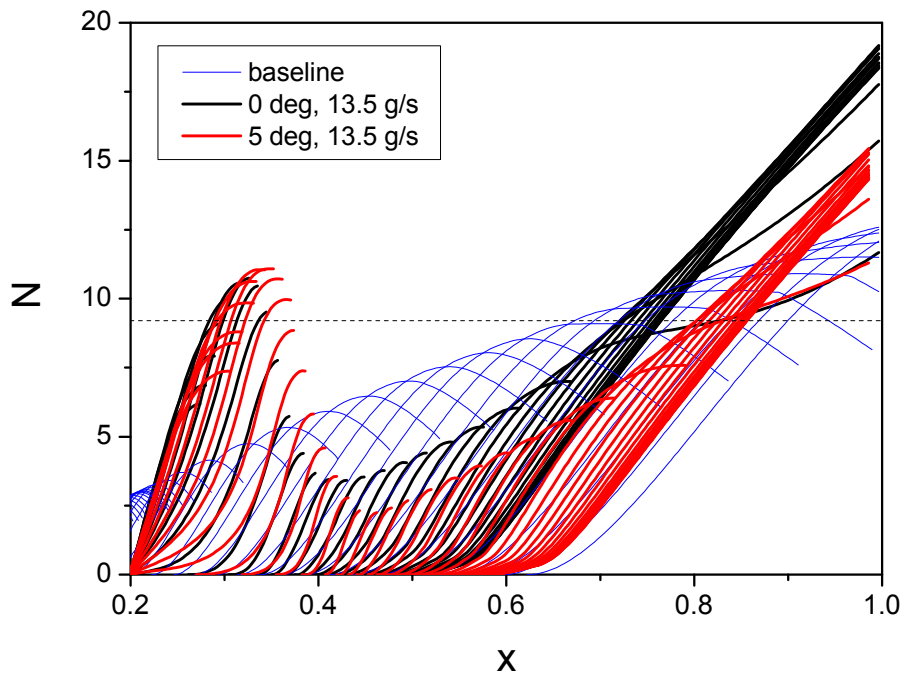
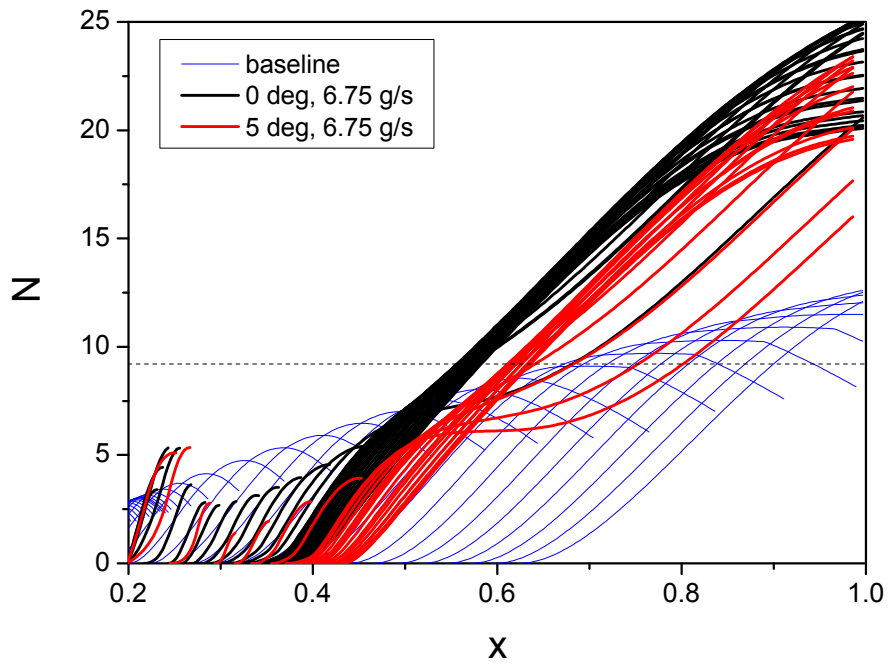


Figure 32 N-factors of the Mack mode for the straight cone with zero blowing (blue lines), for the injector of $\Delta\theta = 0^\circ$ (black lines) and for the cylindrical injector of $\Delta\theta = 5^\circ$ (red lines). For the upper plot the injected mass flow rate is $\dot{m} = 6.75$ g/s, and for the lower plot $\dot{m} = 13.5$ g/s; dashed line – $N_{tr} = 9.2$.

3.3 Cylindrical-conical injector

Consider the cylindrical-conical (CC) injector of the shape schematically shown in Fig. 19. The gas blowing is performed in the region from $x_1 = 0.128$ to $x_2 = 0.169$. It was expected that this configuration helps to reduce the thickness of dead-flow layer downstream from the injector. It was also expected that acceleration of the near-wall flow in the vicinity of $x = x_2$ may help to stabilize the boundary layer in the near-field relaxation region and, thereby, improve the injector performance. To examine these presumptions we have computed the mean flow and the second-mode growth rates for the case of the dimensionless mass flow rate $\rho_w v_w = 0.021$ that approximately corresponds to the total mass flow rate $\dot{m} = 13.5$ g/s. Close-up views of the pressure and axial velocity fields are shown in Figs. 33 and 34, respectively. Comparing these fields with the case of cylindrical injector (Figs. 26 and 27) we conclude that the CC shape leads to the significant increase of pressure perturbation, while the boundary-layer thickness is reduced in the relaxation region (see Fig. 35).

The nondimensional maximal (vs. frequency) growth rates of the Mack mode are shown in Fig. 36. Despite significant differences in the mean flow characteristics, $\sigma_{\max}(x)$ for the CC injector is not so far from the case of cylindrical injector (compare the green and red lines). As shown in Fig. 37, the dimensional growth rates at various fixed frequencies are affected in the two different ways. The CC shape leads to the reduction of maximal $\sigma^*(x)$ and the increase of the unstable region length. As a result, the N factor envelope for the CC injector is higher than in the case of cylindrical injector. Thus, we conclude that the CC shape considered does not improve the injector performance at $\dot{m} = 13.5$ g/s.

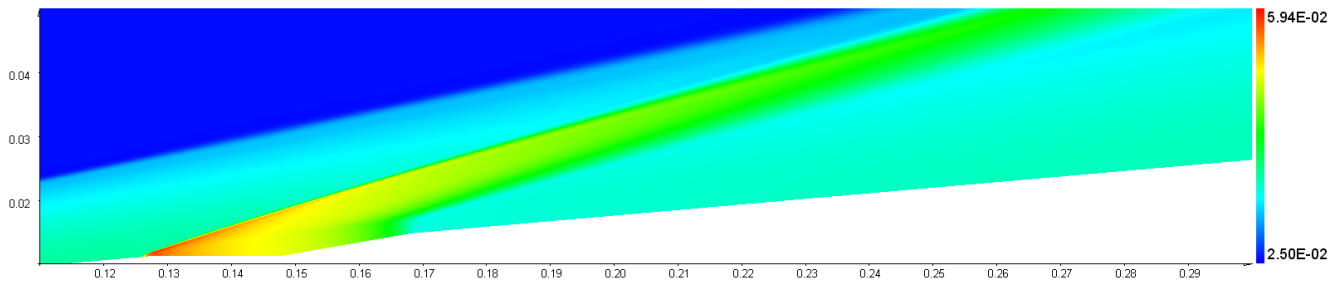


Figure 33 Static pressure in the region $0.11 < x < 0.3$, $\dot{m} = 13.5$ g/s.

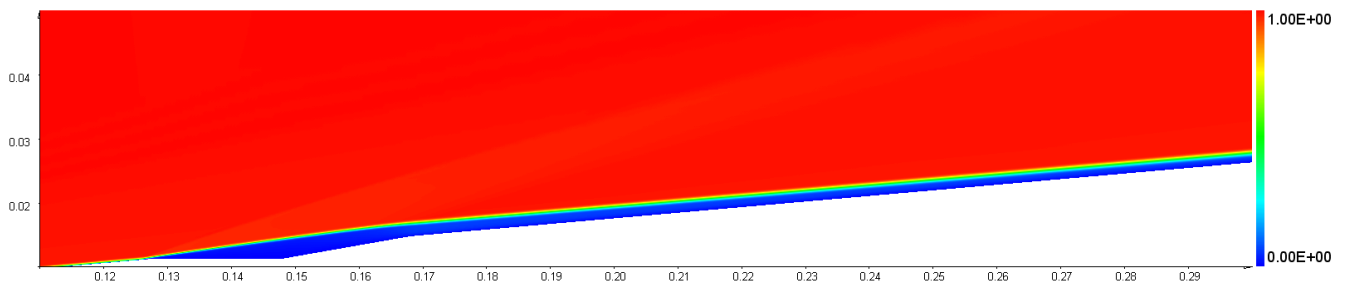


Figure 34 Axial velocity in the region $0.11 < x < 0.3$, $\dot{m} = 13.5$ g/s.

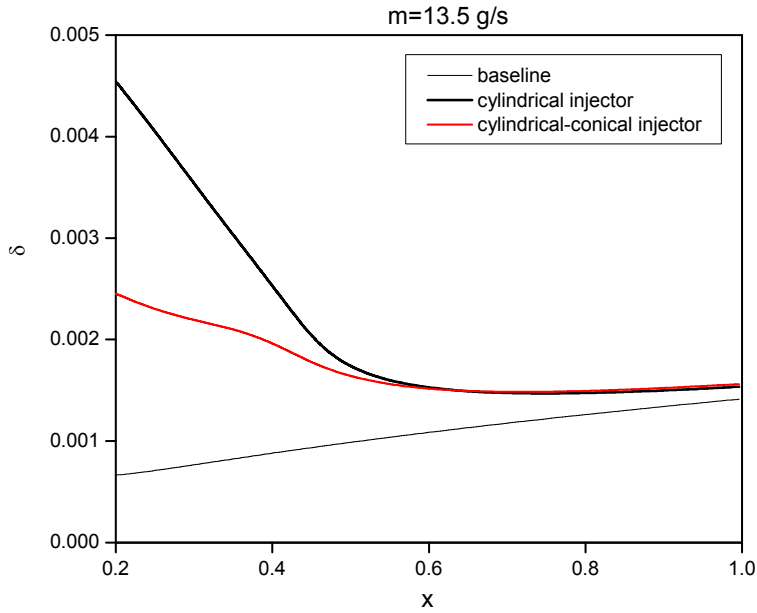


Figure 35 Distributions of the boundary-layer thickness for the cylindrical injector and the cylindrical-conical injector, the total mass rate is $\dot{m} = 13.5$ g/s.

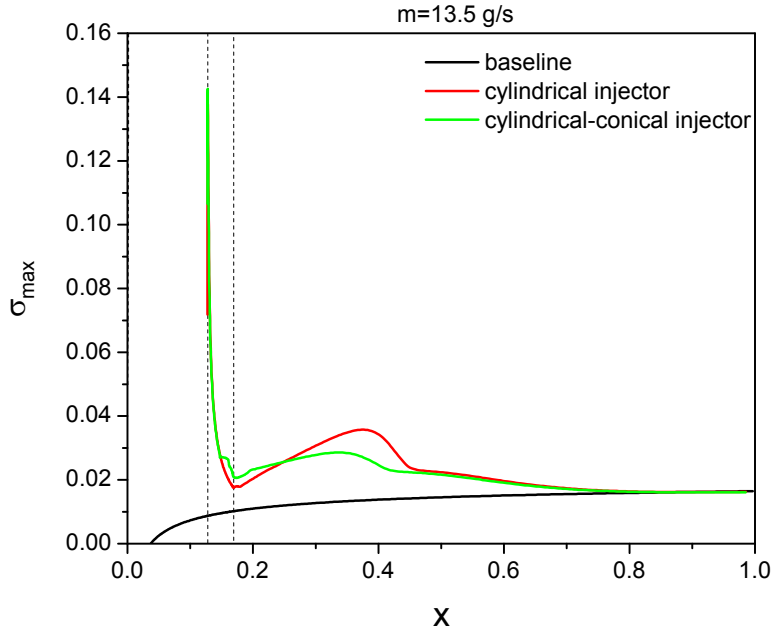


Figure 36 Maximal (vs. frequency) growth rates of the Mack mode. Black line – baseline case of straight cone with zero injection; red line – cylindrical injector, green line – cylindrical-conical injector at $\dot{m} = 13.5$ g/s. Dashed lines show the boundaries of injection. σ_{\max} is made nondimensional using the Blasius length scale $\sqrt{\nu_e^* x^* / U_e^*}$.

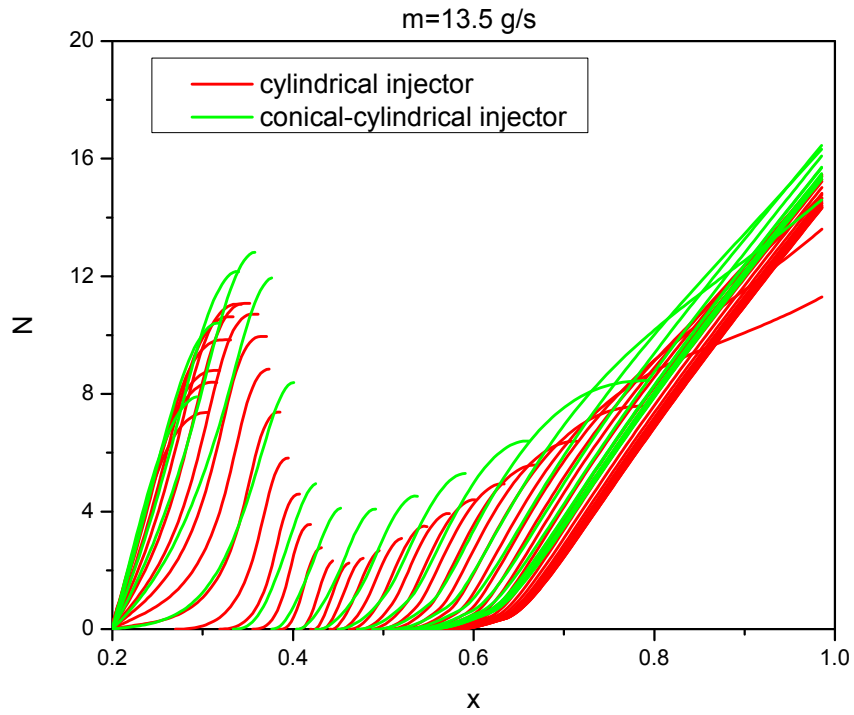
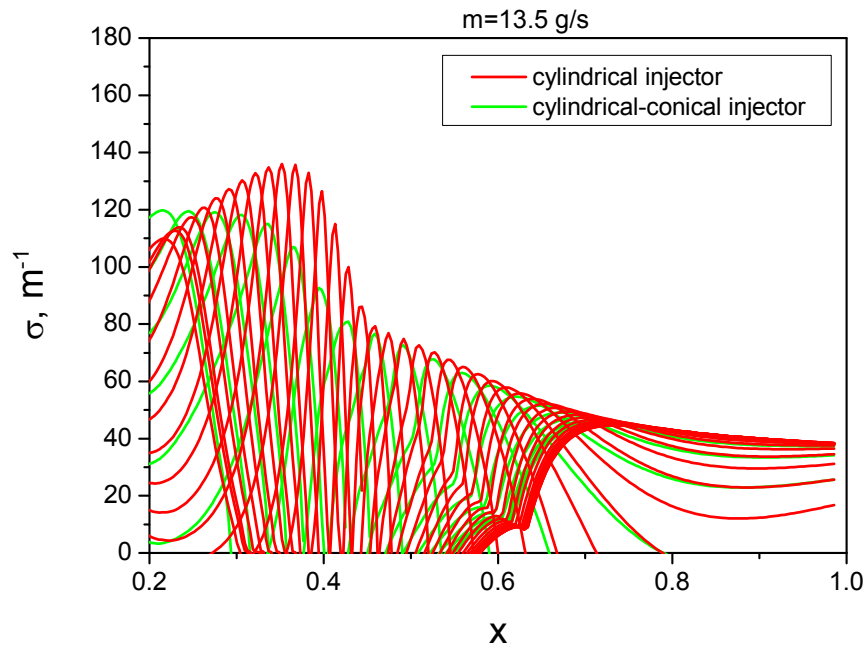


Figure 37 Growth rates and N-factors of the Mack mode for the cylindrical injector (red lines) and the cylindrical-conical injector (green lines) at $\dot{m} = 13.5 \text{ g/s}$.

4. Suction-blowing of zero total mass injection

Another way to improve the injector performance could be a combination of normal-wall suction and blowing with zero net injection as schematically shown in Fig. 38. It is expected that the preliminary suction of the incoming boundary-layer flow could partially compensate negative effects produced by the subsequent blowing.

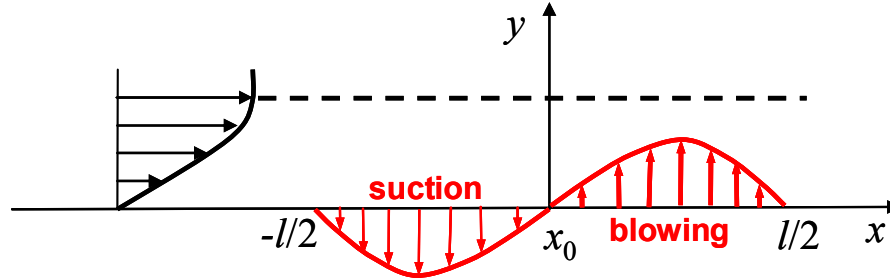


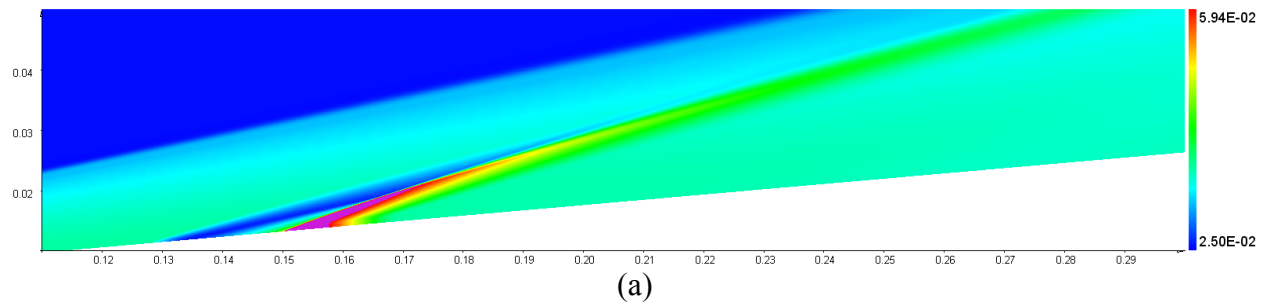
Figure 38 Schematics of suction-blowing of zero net injection.

This expectation is examined by stability computations for the following distribution of suction-blowing. In the region $-l^*/2 \leq x^* - x_0^* \leq l^*/2$, where $x_0^* = 212.5$ mm is the injector center and $l^* = 41$ mm, the dimensionless mass flow rate $q = \rho_w v_w$ is specified as

$$q(\varphi) = q_0 \sin \varphi, \varphi = (x^* - x_0^*)2\pi / l^*, \quad -\pi \leq \varphi \leq \pi. \quad (2)$$

Computations were performed for the total mass rate $\dot{m}_+ = 6.75$ g/s in the blowing region $x_0^* < x^* < l^*/2$ (a half of the maximal injection mass rate considered in the previous sections). The mean flow field for static pressure, axial velocity and temperature are shown in Fig. 39. Figure 40 compares the wall pressure distributions for the baseline (no-blow) case, the uniform blowing case of $\dot{m} = 6.75$ g/s and the suction-blowing case of $\dot{m}_+ = 6.75$ g/s. It is seen that in the suction-blowing case the relaxation region is shorter and the dead-flow layer is thinner than in the case of uniform blowing. However the local perturbations in the vicinity of the suction-blowing system are relatively large.

Figure 41 shows the N factors corresponding to the cases depicted in Fig. 40. As contrasted to the original expectation, the suction-blowing system destabilizes the flow compared with the uniform blowing case. Thus, the preliminary suction does not improve the injector performance.



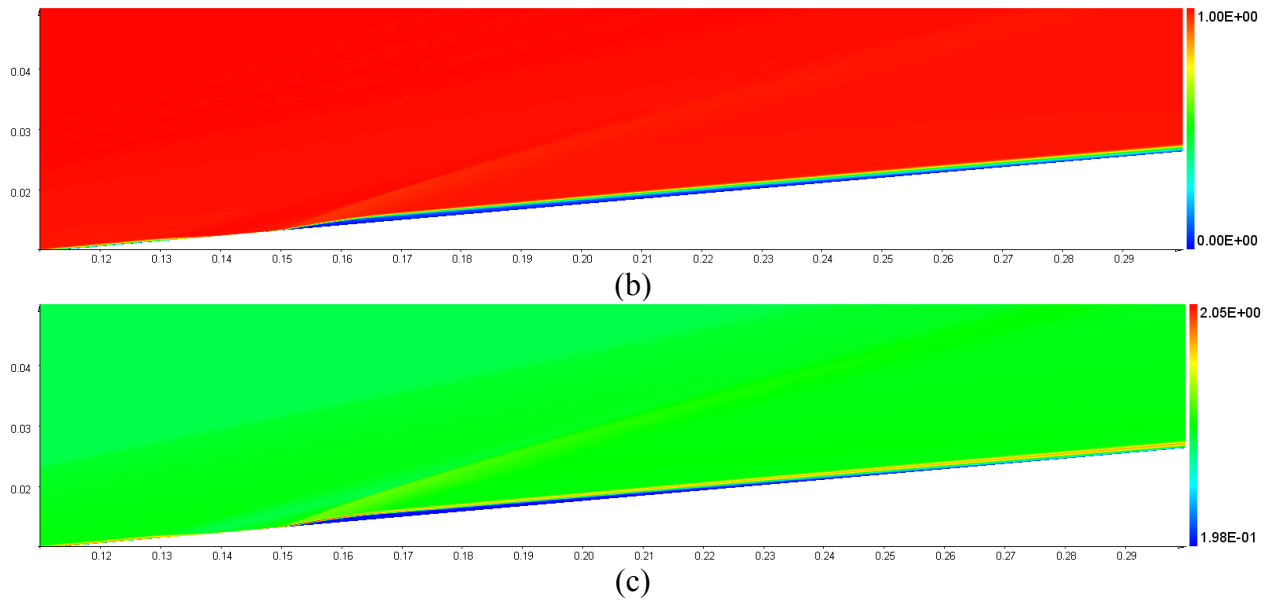


Figure 39 Basic flow fields for the static pressure (a), axial velocity (b), and temperature (c) at $\dot{m}_+ = 6.75$ g/s.

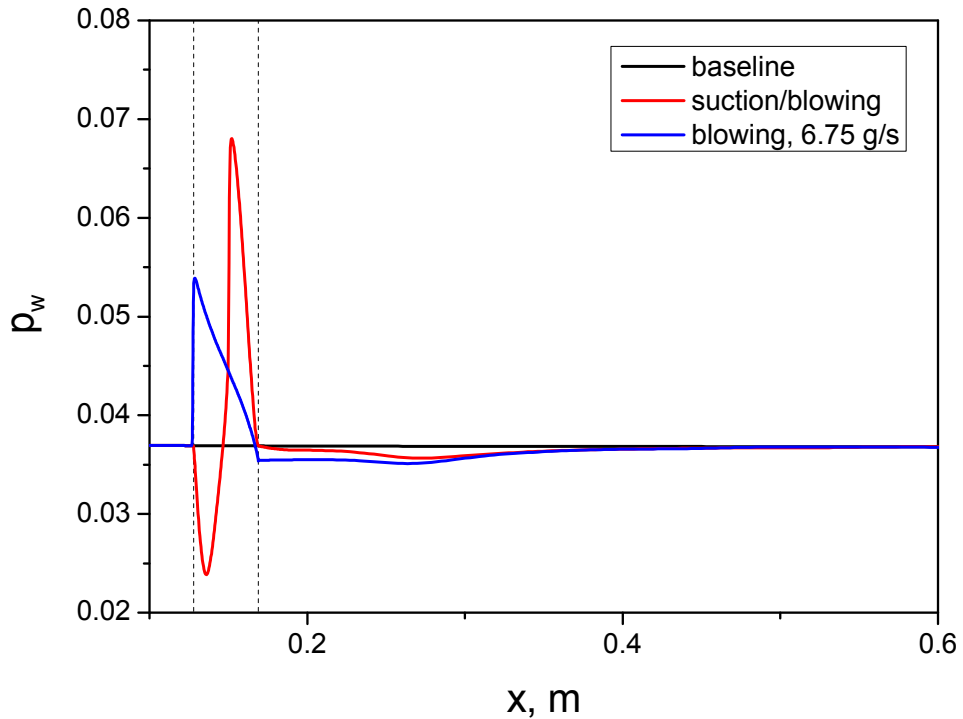


Figure 40 The wall pressure distributions for the baseline (no blow) case (black line), the uniform blowing of $\dot{m} = 6.75$ g/s (blue line) and the suction-blowing of $\dot{m}_+ = 6.75$ g/s (red line).

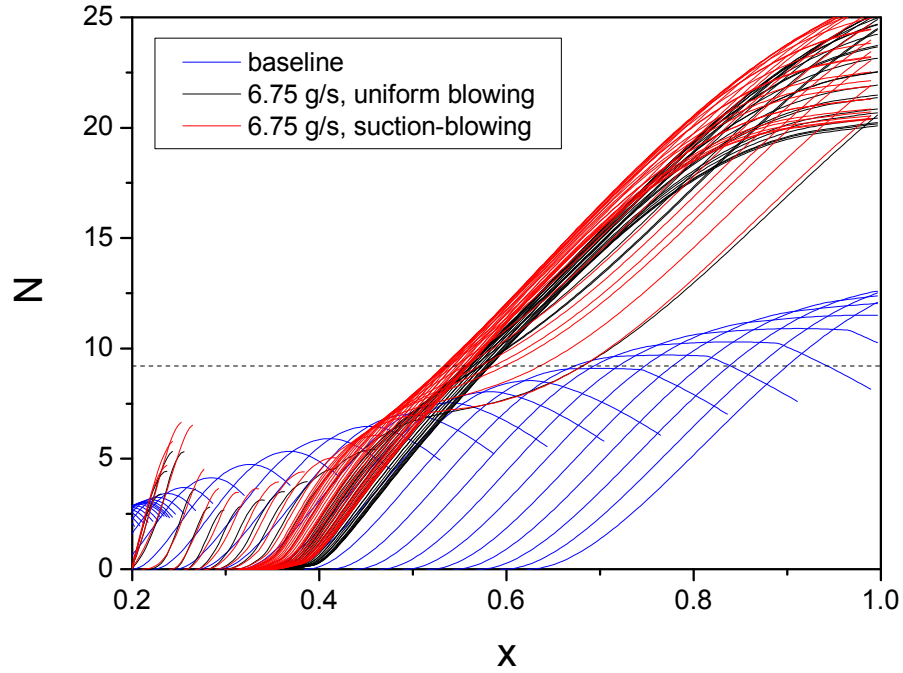


Figure 41 N-factors of the Mack mode for the baseline (no-blow) case (blue lines), the uniform blowing case of $\dot{m} = 6.75$ g/s (black line) and the suction-blowing case of $\dot{m}_+ = 6.75$ g/s (red line); dashed line – $N_{tr} = 9.2$.

5. Porous wall effect

In this section we consider the porous wall effect on the Mack mode instability. In accord with the model developed in Ref. [13] the spatial stability problem is solved with the impedance boundary conditions for disturbances on the porous wall

$$v_w = Ap_w, \quad (3)$$

where v is the vertical velocity disturbance, p is the pressure disturbance. The acoustic admittance A depends on the porous layer microstructure. The porous wall of the injector considered herein was fabricated from sintered 316L stainless steel with the media grade of 10 μm . This wall has a random porosity of the average pore size $d^* \approx 10$ μm . The porous layer thickness $h^* = 1.6$ mm is much larger than d^* . The top view of the injector surface is shown in Fig. 42. For the first-cut evaluation of the porous wall effect, we assume that the acoustic admittance of the actual porous layer is close to that of a porous layer with regular microstructure. Namely, we consider a porous wall with equally spaced vertical cylindrical micro-holes. Its admittance is expressed in the analytical form derived in Ref. [13]. For $h \gg d$, we get

$$A = -\phi / Z_0, \quad (4)$$

where ϕ is porosity. The characteristic impedance Z_0 is expressed in terms of the complex dynamic density and the complex compressibility, which are calculated using analytical solutions for acoustic disturbances propagating within a long cylindrical pore of radius r_p^* .

In the following stability computations, the pore radius is $r_p^* = 5 \text{ }\mu\text{m}$ (a half of the media grade), and porosity $\phi = 0.2$ corresponds to the pore spacing $4r_p^*$. The porous coating covers the cone surface from the injector to the cone base. The free-stream parameters correspond to Run 2540 – they are specified in Section 2.

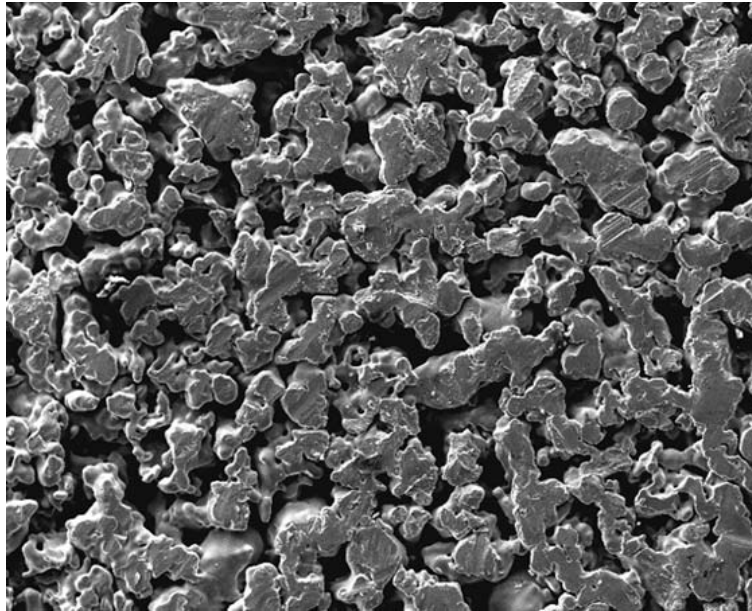


Figure 42 Magnified image of the porous surface for the injector tested in the T5 shock tunnel.

5.1 Porous coating for the baseline configuration

First we consider the baseline configuration A without injection. The growth rate distributions $\sigma^*(x)$ of the Mack mode at various frequencies are shown in Fig. 43. The corresponding N-factors are plotted in Fig. 44. It is seen that the porous wall produces a strong stabilization effect for the all frequencies considered. In the porous wall case, the N-factor envelope lies well below the critical level $N_{tr} = 9.2$ suggesting that the boundary layer flow should be laminar all of the way to the end of the cone.

Our estimates show that the pore radius is small compared with the viscous Stokes layer forming on the pore surface for the all frequencies considered. Due to viscous dissipation the boundary-layer disturbances quickly vanish inside each pore that provides effective absorption of the acoustic energy and, thereby, stabilization of the boundary-layer flow.

The foregoing model assumes that:

- The number of pores per the instability wavelength (n_{por}) is large (this allows us to average the boundary condition over the porous surface)

- Roughness of the pore surface is negligible – the surface is treated as aerodynamically smooth

To check the first assumption we have calculated $n_{por}(x)$ using the wavelength distribution $\lambda^*(x)$ for the most unstable (vs. frequency) waves. Figure 45 shows that $n_{por} > 100$ downstream from the injector ($x > 0.2$). To check the second assumption we have calculated the roughness Reynolds number [17]

$$Re_{kk} = \frac{U^*(k^*)k^*}{\nu^*(k^*)} \approx \frac{U_w^{*'}k^{*2}}{\nu^*(T_k^*)}, T_k^* \approx T_w^* + T_w^{*'}k^*, \quad (5)$$

where k^* is the roughness height, which is estimated as $k^* \approx d^* = 10 \mu\text{m}$. Figure 46 shows that in the region $0.1 < x < 1$ the roughness Reynolds number is essentially smaller than the conservative criterion $Re_{kk} = 25$ for distributed roughness [18]. Thus, the both assumptions are valid for the porous layer microstructure considered.

Now we consider the case of injection with $\dot{m} = 13.5 \text{ g/s}$. As in the case considered in Section 2, the gas blowing is performed in the region $128 \text{ mm} < x^* < 169 \text{ mm}$. Further downstream the cone surface is assumed to be covered by the passive porous layer. The stability computations were conducted in the range of $0.2 \text{ m} < x^* < 1 \text{ m}$ - downstream from the injector. Figure 47 compares the growth rate distributions $\sigma^*(x)$ for the case with the porous coating (red lines) and without it (black lines). The corresponding N-factors are compared in Fig. 48. As expected the porous coating leads to significant stabilization of the Mack mode.

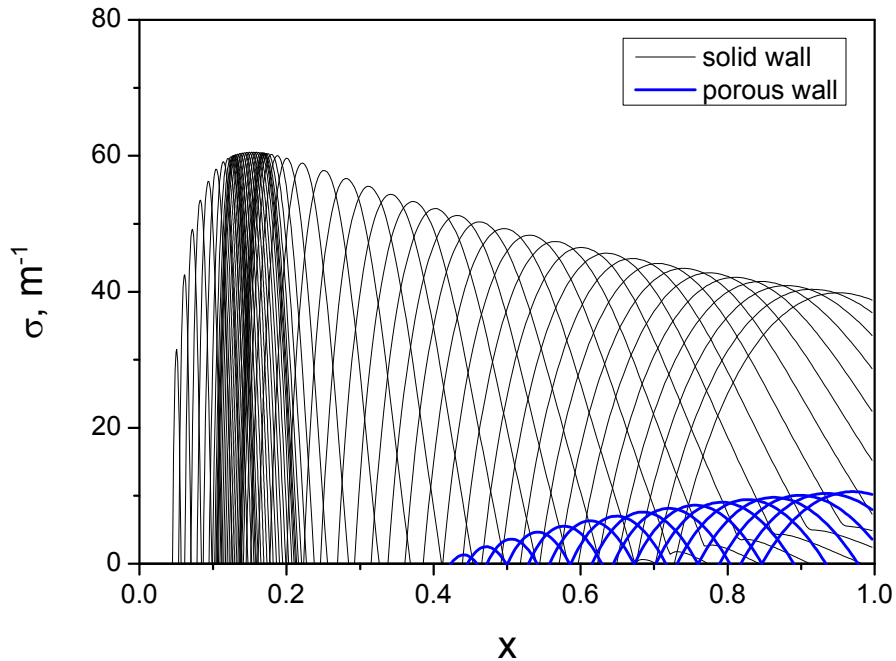


Figure 43 Growth rates $\sigma^*(x)$ of the Mack mode at various frequencies; black lines – solid wall, blue lines – porous wall; there is no injection.

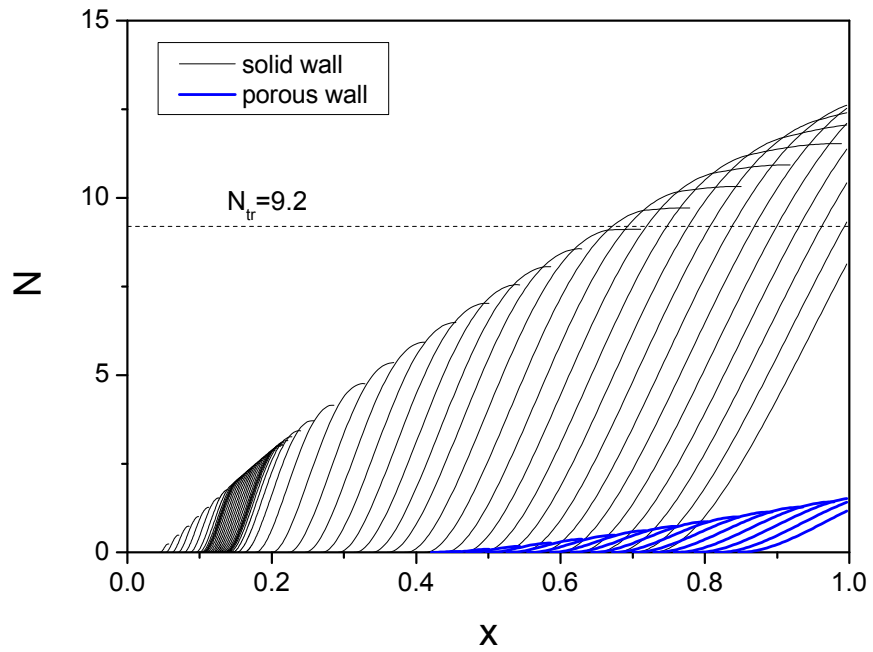


Figure 44 N-factors of the Mack mode at various frequencies; black lines – solid wall, blue lines – porous wall; there is no injection.

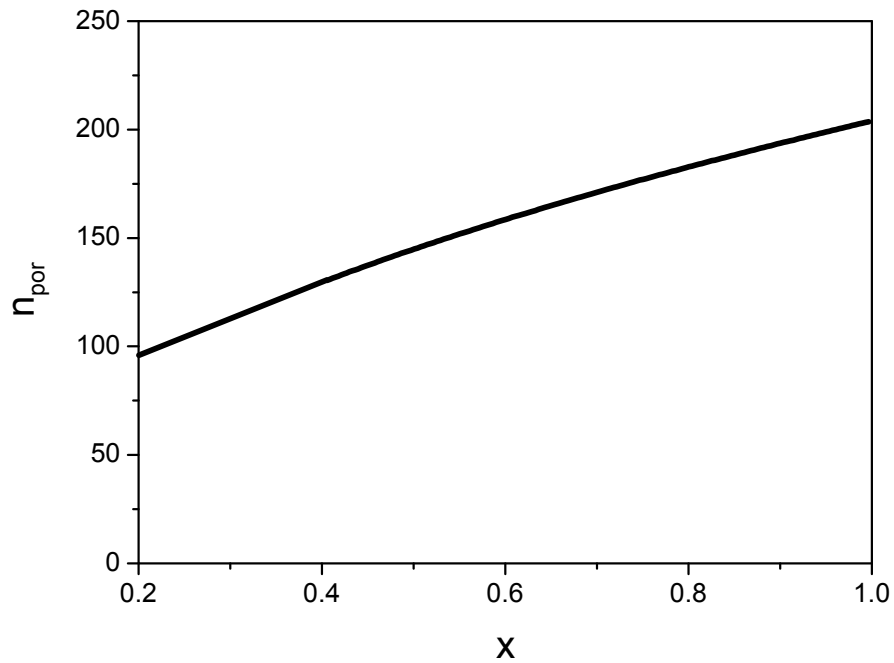


Figure 45 The number of pores per the instability wavelength $n_{por}(x)$.

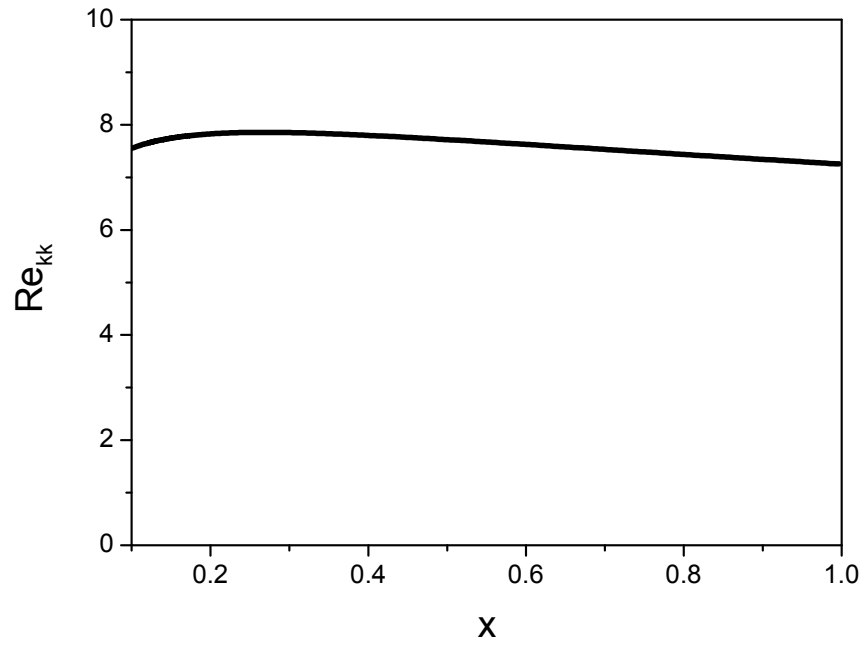


Figure 46 The Reynolds number distribution $Re_{kk}(x)$ at $k^* = 10 \mu\text{m}$.

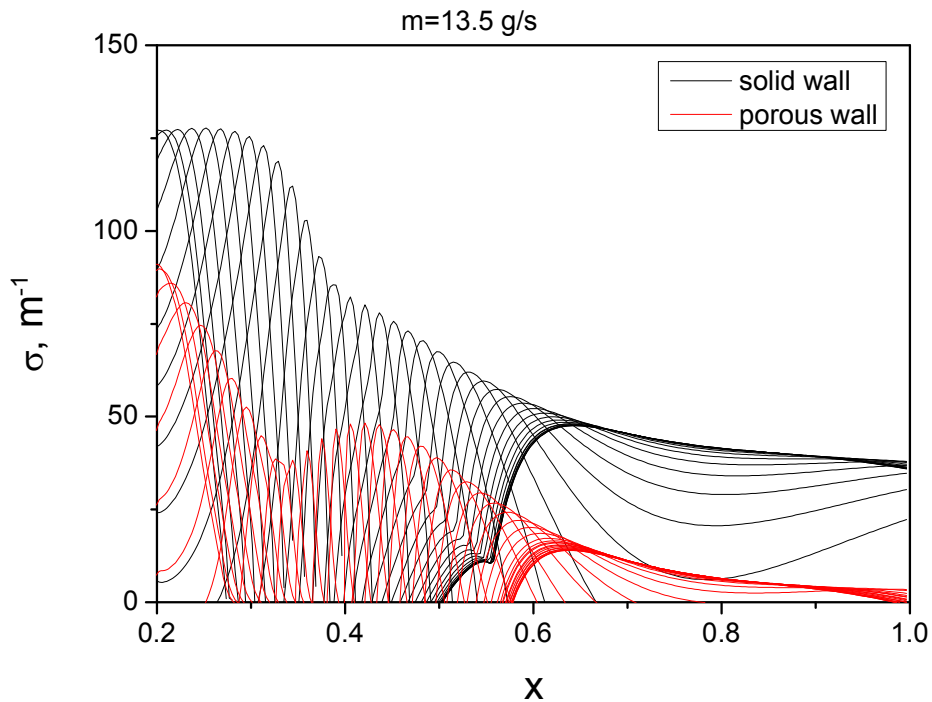


Figure 47 The Mack mode growth rates $\sigma^*(x)$ at various frequencies in the case of injection with $\dot{m} = 13.5 \text{ g/s}$; black lines – solid wall, red lines – wall with the porous coating.

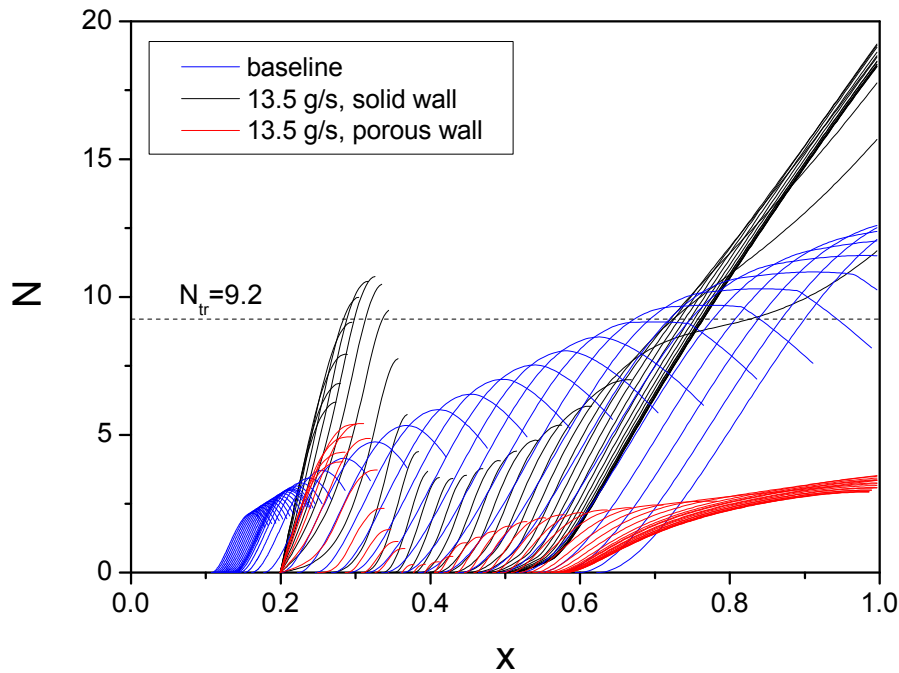


Figure 48 N-factors of the Mack mode at various frequencies in the case of injection with $\dot{m}_i = 13.5$ g/s; black lines – solid wall, red lines – wall with the porous coating.

This numerical example indicates that the CO₂ injector performance can be improved using the following approach. The porous layer, which is used for the injection, should be protruded downstream to the near-field relaxation region as schematically shown in Fig. 49. The protruded portion is placed on the solid backup and it works as a passive porous coating (there is no suction or blowing through this coating). In the case considered, the protruded portion should cover the cone surface from $x^* = 169$ mm to approximately $x^* \approx 300$ mm. This may help to reduce the first maximum of the N-factor envelope and, thereby, avoid premature transition. Further downstream, the CO₂ stabilization effect is expected to be sufficiently strong to keep the boundary-layer flow laminar.

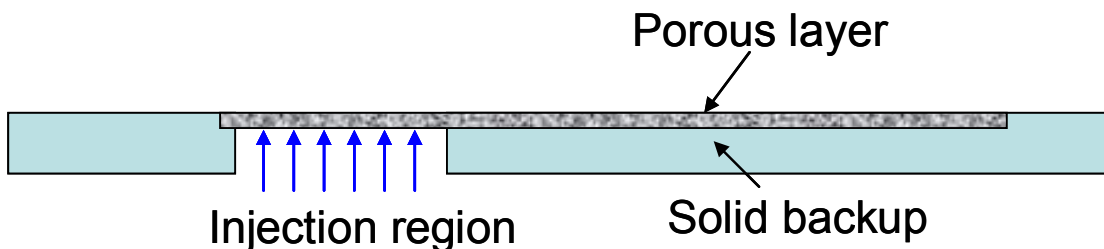


Figure 49 Schematics of the injector with UAC. The porous layer is protruded downstream from the injection region to cover the near-field relaxation region. The protruded part is placed on a solid backup

6. Conclusions

Stability analyses of high-speed boundary-layer flow past a 5° half angle sharp cone with the wall-normal injection of gas through a porous strip were performed using Navier-Stokes solutions for the mean flow and the linear stability theory. The cone model and free-stream parameters were chosen to be similar to the experiments, which were carried out at Caltech's T5 shock tunnel to investigate the effect of CO_2 injection on laminar-turbulent transition.

It was found that the injection induces a cold dead-flow layer, which is slowly swallowed by the shear layer in the downstream relaxation region. The near-wall flow behaves as a wave guide which can support several unstable modes of acoustic type. The spatial stability analysis showed that the most unstable mode corresponds to the Mack second mode. The phase speeds of this instability are close to the phase speeds of slow acoustic waves, and its frequencies are several times smaller than in the no injection case. This may lead to significant increase of receptivity to free-stream acoustic noise.

The e^N computations showed that the injection leads to destabilization of the near-field relaxation region, stabilization of the mid-field relaxation region, and destabilization of the far-field relaxation region where the basic flow is almost parallel. The width and location of these regions as well as the level of stabilization/destabilization effect essentially depend on the injected mass flow rate. These results are consistent with the stability computations of Wagnild et al. [7], which were carried out for CO_2 injection including the real-gas effects. This convinces us that the perfect gas modeling can be used for a first-cut evaluation of the injector performance.

In order to improve the injector performance it was suggested to decrease the injector surface slope. It was suspected that this shaping could partially compensate the displacement effect induced by the injection and thereby reduce the instability growth in the near-field relaxation region. However, the e^N parametric studies predicted that this shaping does not stabilize the near-field flow and, therefore, it does not prevent from early transition at sufficiently large injection rates. For relatively small \dot{m} at which the N-factors in the near-field relaxation region are below the critical level, the shaping produces a significant stabilization effect in the mid- and far-field relaxation regions. It is expected that this stabilization will be enhanced by the injection of CO_2 .

Stability computations were also conducted for the injector of cylindrical-conical (CC) shape at the total injection rate $\dot{m} = 13.5$ g/s. It was found that the CC shape leads to the reduction of maximal growth rates and the increase of the unstable region length. As a result, the N factor envelope for the CC injector is higher than in the case of cylindrical injector – the CC shape considered does not improve the injector performance.

Apparently, the foregoing shaping is not exhaustive. Additional parametric studies are needed to identify an optimal shape at which the injector does not cause premature transition in the near-field relaxation region.

It was suspected, that the injector performance could be improved using a combination of normal-wall suction and blowing with zero net injection. It was assumed that the preliminary suction of the incoming boundary-layer flow could partially compensate negative effects produced by the subsequent blowing. However, the e^N computations showed that the suction-blowing system destabilizes the flow in the whole relaxation region compared with the case of blowing at $\dot{m} = \dot{m}_+ = 6.75$ g/s.

The porous wall effect on the acoustic instability was also examined using the linear stability theory with the impedance boundary conditions on the porous surface. It was found that porosity strongly stabilizes the boundary layer flow with and without injection. This suggests that the injector performance can be improved, if the porous layer, which is used for the injection, is protruded downstream to cover the near-field relaxation region. This will help to reduce the first maximum of the N-factor envelope and, thereby, avoid premature transition. Further downstream, the CO₂ stabilization effect is expected to be sufficiently strong to keep the boundary-layer flow laminar.

It should be noted that the local injection induces spatial non-uniformities of the basic flow, which can alter the instability growth rates via nonparallel effects. Because our stability analysis does not account for these effects, the foregoing results should be taken with great caution. The PSE analysis and direct numerical simulations are needed to verify the e^N predictions reported herein. Note also that the perfect gas model does not account for the CO₂ stabilization effect owing to absorption of acoustic energy. This model is suitable for the near-field region where the injected gas is relatively cold and the absorption effect is weak. Further downstream, where the injected flow is heated, the perfect gas model overestimates the disturbance growth rates and, presumably, under-predicts the injector performance. Nevertheless, the perfect gas modeling provides a good launching pad for further stability analysis including the real gas effects.

References

1. Mack, L.M., "Boundary-layer stability theory," In Special Course on Stability and Transition of Laminar Flow, AGARD Report Number 709, 1984.
2. Fedorov, A., "Transition and Stability of High-Speed Boundary Layers," *Annu. Rev. Fluid Mech.*, Vol. 43, 2011, pp. 79-95.
3. Lighthill, M.J., Viscosity effects in sound waves of finite amplitude. In G.K. Batchelor and R.M. Davies, editors, *Surveys in Mechanics*, pp. 250-351. Cambridge University Press, 1956.
4. Vincenti, W.G. and Kruger, C.H. *Introduction to Physical Gas Dynamics*, Krieger Publishing Company, 1965.
5. Fujii, K., and Hornung, H. G., "Experimental Investigation of High Enthalpy Effects on Attachment-line Boundary Layer Transition," *AIAA J.*, Vol. 41, No. 7, July 2003.
6. Leyva, I. A., Jewell, J. S., Laurence, S., Hornung, H. G., Shepherd, J. E., "On the Impact of Injection Schemes on Transition in Hypersonic Boundary Layers," AIAA-2009-7204, October 2009.
7. Wagnild, R.M., Candler, G.V., Leyva, I.A., Jewell, J.S., and Hornung, H.G., "Carbon Dioxide Injection for Hypervelocity Boundary Layer Stability," AIAA-2010-1244, January 2010.
8. Jewell, J.S., Leyva, I.A., Parziale, N.J., and Shepherd, J.E., "Effect of Gas Injection on Transition in Hypervelocity Boundary Layers," ISSW, July 2011.
9. Egorov, I.V., Fedorov, A.V., and Soudakov, V.G., "Direct Numerical Simulation of Disturbances Generated by Periodic Suction-Blowing in a Hypersonic Boundary Layer," *Theor. Comput. Fluid Dyn.*, Vol. 20, No. 1, 2006, pp. 41-54.
10. Egorov, I.V., Fedorov, A.V., and Soudakov, V.G., "Receptivity of a hypersonic boundary layer over a flat plate with a porous coating," *J. Fluid Mech.*, Vol. 601, 2008, pp. 165-187.

11. Fedorov, A.V., Soudakov, V.G., and Egorov, I.V., "Investigations of laminar-turbulent transition on a sharp cone with localized heating or cooling in high-speed flow," AIAA-2013-0524, January 2013.
12. Fedorov, A.V., "Theoretical modeling of TS-dominated transition induced by solid particulates," AIAA-2013-668, January 2013.
13. Fedorov, A.V., Malmuth, N.D., Rasheed, A., and Hornung, H.G., "Stabilization of Hypersonic Boundary Layers by Porous Coatings," *AIAA J.*, Vol. 39, No. 4, 2001, pp. 605-610.
14. Rasheed, A., Hornung, H.G., Fedorov, A.V., and Malmuth, N.D., "Experiments on Passive Hypervelocity Boundary Layer Control Using an Ultrasonically Absorptive Surface," *AIAA J.*, Vol. 40, No. 3, 2002, pp. 481-489.
15. Brès, G.A., Inkman, M., Colonius, T., and Fedorov, A.V., "Second-Mode Attenuation and Cancellation by Porous Coatings in a High-Speed Boundary Layer," *J. Fluid Mech.*, Vol. 726, 2013, pp. 312-337.
16. Jiang, G.-S., and Shu, C.-W., "Efficient Implementation of Weighted ENO Schemes," *J. Comput. Phys.*, Vol. 126, 1996, pp. 202-228.
17. Reda, D.C., "Review and synthesis of roughness-dominated transition correlations for reentry applications," *J. Spacecraft and Rockets*," Vol. 39, No. 2, 2002, pp. 161-167.
18. Schneider, S.P., "Effects of roughness on hypersonic boundary-layer transition," *J. Spacecraft and Rockets*, Vol. 45, No. 2, 2008, pp. 193-209.